

Stability of hydrotalcite (Mg-Al layered double hydroxide) in presence of different anions

Ellina Bernard^a, Wolfgang Jan Zucha^{b,*}, Barbara Lothenbach^{b,c}, Urs Mäder^a

^a University of Bern, Institute of Geological Sciences, Rock Water Interaction Group, 3012 Bern, Switzerland

^b University of Bern, Institute of Geological Sciences, Mineralogy Group, 3012 Bern, Switzerland

^c Laboratory for Concrete & Asphalt, Swiss Federal Laboratories for Materials Science and Technology (Empa), 8600 Dübendorf, Switzerland

ARTICLE INFO

Keywords:

Hydrotalcite

LDH

Magnesium

Anions

Thermodynamic data

ABSTRACT

MgO contained in cementitious materials is experimentally observed to precipitate as poorly crystalline hydrotalcite (Mg-Al LDH). However, the geochemical modelling of hydrotalcite is challenging due to the lack of consistent thermodynamic dataset for this phase. Hydrotalcites with Mg/Al = 2 were synthesised in the presence of NaHCO₃, NaCl, Na₂SO₄, NaNO₃, and NaOH. Mass balance, XRD and FT-IR indicated the incorporation of the anions in the interlayer together with some carbonate. The crystallinity of the phase increased depending on the anion: SO₄²⁻ < Cl⁻ < NO₃⁻ < OH⁻ < CO₃²⁻. An in-situ increase of temperature monitored by XRD and TGA showed that the stability of the hydrotalcite structure with temperature also depended on the incorporated anion. The solubility products were calculated based on the solution analysis of samples re-equilibrated at different temperatures, while the entropy and heat capacity were obtained from the additivity method or the molar volume. A simple solid-solution model for hydrotalcite containing CO₃, OH, SO₄, Cl and NO₃ is suggested.

1. Introduction

In the context of lowering the 5 to 8% anthropogenic CO₂ emissions from cement industry [1], particularly from the Portland cement manufacture, alternative binders or partial replacement of the clinkers by so called supplementary cementitious materials (SCMs) are studied. The use of reactive aluminosilicate containing SCMs, such as fly ash, blast furnace slag or calcined clays, increases the aluminium and silicate content, which can affect the phase composition in the hydrated cement and increase the Al and Si incorporation into the calcium (alumino-) silicate phases (C-(A-)S-H) [2]. Also, the content of magnesium is expected to raise in future CO₂-reduced clinkers, either from the use of blast furnace slag or of magnesium silicate minerals. Magnesium from slags or from other MgO sources is observed to precipitate as hydrotalcite, i.e. a Mg-Al layered double hydroxide (LDH) [3–9], although its exact composition often remains unclear.

Hydrotalcite-like phases are Mg and Al based layered double

hydroxide solids (Mg-Al-LDH) with an isomorphic substitution of Mg²⁺ by Al³⁺ in the brucite-like sheet, that generates positive charges in the main layer. The main layer can have a variable Mg/Al ratio [10,11], Al can be replaced by iron [12,13], and different interlayer anions can be contained in the interlayer [10]. The positive charge of the main layer is compensated by anions and water in the interlayer region [14]. Mg-Al-LDH can be written as [Mg_{1-x}Al_x(OH)₂]^{x+} [A_{x/n}ⁿ⁻ mH₂O]^{x-}, with 0 < x < 0.33 [14]; “A” indicates the presence of anions such as OH⁻, Cl⁻, NO₃⁻, CO₃²⁻, SO₄²⁻ in the interlayer. The affinity is CO₃²⁻ > SO₄²⁻ for divalent anions and OH⁻ > F⁻ > Cl⁻ > Br⁻ > NO₃⁻ > I⁻ for monovalent anions [14].

While crystalline LDHs are widely studied and used as catalysts, anion exchangers and adsorbents [15], LDHs precipitate semi-amorphous in cement pastes and the formation of different solid solutions is observed [5]. Not only the incorporation of OH⁻ is detected but also the uptake of chloride and/or carbonate by hydrotalcite which seems to reduce the chloride and carbonation ingresses in hydrated

Abbreviations: ATR FT-IR, attenuated total reflectance Fourier-transform infrared; C-(A-)S-H, calcium (alumino-)silicate hydrate; C_p, heat capacity; FWHM, full width at half maximum; K_{so}, solubility product; LDH, layered double hydroxide; MAS NMR, magic-angle spinning nuclear magnetic resonance; M-(A-)S-H, magnesium (alumino-)silicate hydrate; Mg-Al-LDH, Mg and Al based layered double hydroxide = hydrotalcite; PC, Portland cement; S°, entropy; SCMs, supplementary cementitious materials; SSA_{BET}, specific surface area obtained by using the Brunauer-Emmett-Teller equation; TGA-FT-IR, thermogravimetric analysis complemented with Fourier Transform Infrared detection of evolved gases; V_{cell}, cell volume; V°, molar volume; XRD, X-ray powder diffraction.

* Corresponding author.

E-mail address: wolfgang.zucha@igt.baug.ethz.ch (W.J. Zucha).

<https://doi.org/10.1016/j.cemconres.2021.106674>

Received 17 May 2021; Received in revised form 5 October 2021; Accepted 14 November 2021

Available online 27 November 2021

This is an open access article under the CC BY license (<http://creativecommons.org/licenses/by/4.0/>).

cements, thus counteracting the potential degradation of reinforcement in concrete [16,17]. An uptake of SO_4^{2-} by hydrotalcite at the interface of cement in direct contact with Opalinus Clay might be possible [18,19], as well as the formation of hydrotalcite conceivably containing NO_3^- in the presence of magnesium aluminium silicate hydrates [20].

The variable composition both in terms of Mg/Al and Mg/(Al + Fe) ratio in the main layer and of interlayer anions of the Mg-Al LDHs in cement pastes, hindered the development of adequate thermodynamic data for hydrotalcites, limiting the use of thermodynamic approaches for studying the magnesium precipitation in the cement pastes. In Cemdata2018 chemical thermodynamic database [21] two different Mg-Al LDHs were considered: for Portland cement (PC) a relatively stable OH-hydrotalcite with a fixed composition is suggested, while for alkali activated slags a series hydroxide LDHs [7] with variable Mg/Al and a different stability are suggested. The carbonated LDHs suggested by [12] were not found to be stable under any condition investigated leading to the estimation of revised thermodynamic properties of carbonate-hydrotalcites in [22,23]. A recent study suggested variable solubility products for hydrotalcite depending on the pH values used [24]. The use of different models for different situations [21] as well as the definition of pH dependent solubility products [24] suggest a lack of adequate thermodynamic models to capture the variable composition in Mg/(Al + Fe) and anion content.

This study investigates Mg-Al LDHs with a Mg/Al = 2 and different interlayer anions. Mg-Al-LDHs containing NO_3^- , Cl^- , SO_4^{2-} , OH^- and CO_3^{2-} were synthesised, characterised by X-ray powder diffraction (XRD), thermogravimetric analysis complemented with Fourier Transform Infrared detection of evolved gases (TGA- FT-IR), attenuated total reflectance Fourier-transform infrared (ATR FT-IR) spectroscopy and ^{27}Al and ^{23}Na MAS NMR spectroscopies. The structure and the stability of the hydrotalcites containing different anions were also studied by in-situ XRD in a heater-controlled chamber. The samples were re-equilibrated at 7, 23, 40 and 80 °C and for each sample, the solution was analysed and the solubility products were calculated.

2. Materials and methods

2.1. Materials and synthesis

Hydrotalcite (652288 Sigma Aldrich CAS Number: 11097-59-9) was used as a source of MgO and Al_2O_3 , although the composition given on the product was $\text{Mg}_6\text{Al}_2(\text{CO}_3)(\text{OH})_{16}4\text{H}_2\text{O}$, a Mg/Al about 2 was found by SEM/EDS. This commercial hydrotalcite (Ht- CO_3^*) was decarbonated and dehydrated for 5 h at 700 °C to remove physically and chemical bound water as well as carbonate resulting in a reactive amorphous solid magnesium aluminate: $\text{Mg}_4\text{Al}_2\text{O}_9$ (M_3A) as shown in Fig. 1.

The M_3A was added to different solutions containing NaHCO_3 (VWR chemicals, ACS, Reag, purity >99.5%), NaCl (Merck, for analysis, purity >99.5%), Na_2SO_4 (VWR chemicals, ACS, Reag, purity >99.5%), NaNO_3 (Merck, for analysis, purity >99.5%), or NaOH (Merck, pellets for analysis, purity >99.5%) with a liquid/solid mass ratio equal to 10. The solutions were prepared according to the amounts summarized in Table S1, using twice the stoichiometric amount of anions to ensure sufficient incorporation of the anion in the interlayer. These Na-based salt solutions can easily be carbonated and this should be avoided. The samples were equilibrated at 80 °C during 20 days to ensure and to fasten the precipitation. The solutions and solids were separated by vacuum filtration using nylon filters (0.45 μm); the solids were washed with 50/50 (volume) water-ethanol to remove dissolved ions. The samples were dried by freezing with liquid nitrogen under vacuum for 2 days in a freeze dryer. The freeze drying minimizes carbonation as it removes free water efficiently. The samples were kept in desiccator over CaCl_2 saturated solution and KOH in order to keep a relative humidity about 34% and to minimise the carbonation until the solid characterisation.

2 g of different hydrotalcites prepared were put back in 50 mL of milliQ-water and equilibrated at 7, 20, 40 and 80 °C for 6 months to measure their solubility. The liquid/solid separation was performed following the method detailed above. However, the samples were not freeze dried to avoid the removal of interlayer water, but dried in a desiccator over silica gel and KOH solution during 2 weeks in order to minimise the carbonation. The solid was characterised and the

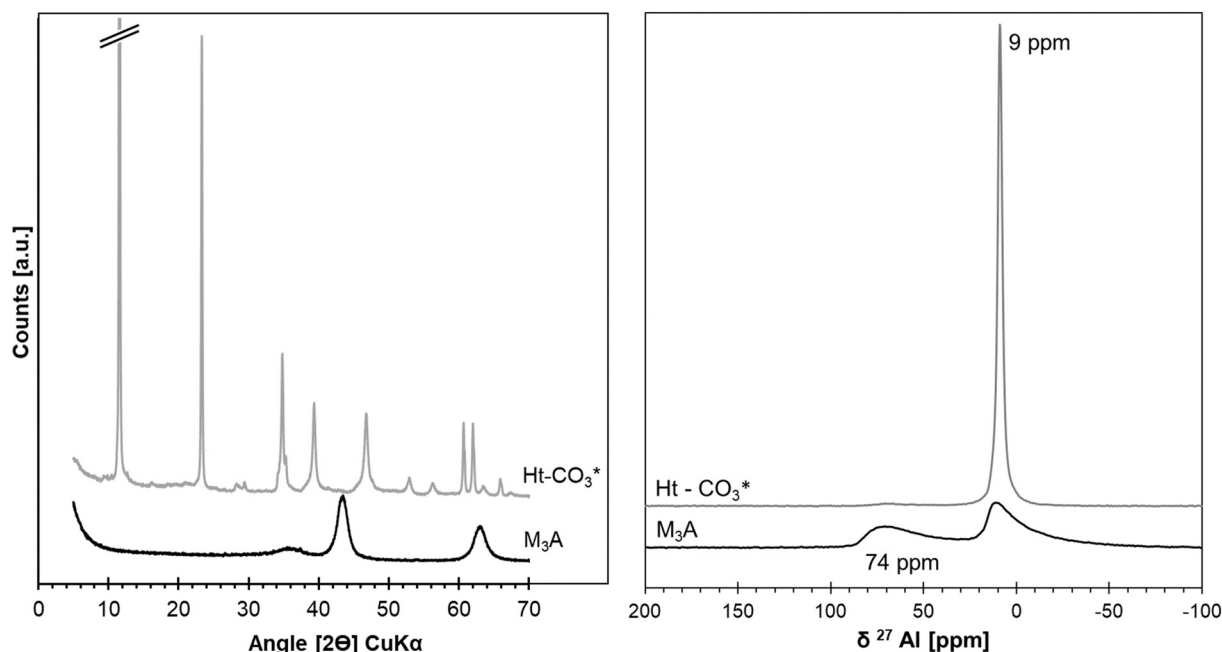


Fig. 1. X-ray diffraction (XRD) patterns (left) and Al NMR spectrum (right) of the commercial hydrotalcite (Ht- CO_3^*) and the heat treated amorphous magnesium aluminate $\text{Mg}_4\text{Al}_2\text{O}_9$ (M_3A).

concentration of the different elements in solution was measured and used to calculate the solubility data at the different temperatures.

2.2. Characterisation techniques

2.2.1. Powder X-ray diffraction

Diffraction data were collected from 5 to 75 2θ with a PANalytical X'Pert Pro MPD diffractometer, equipped with a Cu X-ray source (40 kV, 40 mA) with a fixed divergence slit size and an anti-scattering slit on the incident beam of 0.5° and 1° and an X'Celerator detector. In-situ high-temperature measurement were carried out on samples re equilibrated at 80 °C on the same diffraction device using a heating chamber HTK 1200 N by Anton Paar. Diffraction data for whole pattern analysis were collected from 5 to 70 2θ with a fixed slit (0.25°) and step size of 0.0167 2θ . The heating rate applied was 1°/s. After the target temperature was reached, the sample was given 10 min to equilibrate. Measurement was performed in uneven intervals of 25 °C (25–100 °C), and 20 °C (100–500 °C) plus a final scan at 600 °C. Diffraction data of the 25 °C scan was used to calculate the lattice parameters and cell volume (V_{cell}) in HighScorePlus using the Pawley method. The R_{wp} -value ranged from 7.4–10.3 from the best to the worst fit.

Molar volume in cm^3/mol (V°) was calculated based on the measured diffraction data using Eq. (1) with $Z = 3$ (hexagonal hydroxalcalite), $x = \text{Al}/(\text{Mg} + \text{Al})$, the Avogadro constant $N_A = 6.02 \times 10^{23} \text{ mol}^{-1}$ and V_{cell} expressed in Å:

$$V^\circ = \frac{2 \cdot N_A \cdot V_{\text{cell}} \cdot 10^{-24}}{x} \quad (1)$$

2.2.2. Evolution of the basal spacing of the hydroxalcalite samples with temperature

Measurement settings were 8–16 2θ with a step size of 0.0167 2θ , a scan step time of 17.78 s, and a heating rate of 1°/s. Diffraction data was collected in steps of 1 °C ranging from 100 to 300 °C. The basal spacing, peak intensity and FWHM of each measurement was extracted with a python script using the `savgol_filter` and `curve_fit` functions of the SciPy library. Specimen displacement was corrected using the offset provided by the manufacturer (thermal expansion) and by adjusting the values to the ones obtained from whole pattern analysis.

2.2.2. N_2 -sorption isotherm for specific surface area calculation

Prior to measurements, 40 mg of a sample was dried at 55 degrees overnight in a vacuum using a Microtrac Belprep Vac III. SSA measurements were then carried out using a Microtrac Belsorp Mini X measuring the full isotherm. The specific surface area (SSA_{BET}) was obtained by using the Brunauer-Emmett-Teller (BET) equation [25], in the pressure range from 0.05 to 0.2 P/P_0 .

2.2.3. Thermogravimetric analysis complemented with Fourier Transform-Infrared gas analysis

TGA measurements were carried out using a Netzsch STA 449 F3 Jupiter TGA apparatus coupled with a Bruker Fourier-transform infrared (FT-IR) spectrometer for the analysis of the exhaust gases. Approximately 40 mg of each sample was heated from 30 to 980 °C with a heating rate of 20 °C per minute in 150 μL alumina crucibles. The infrared absorbances of H_2O , N_2O and CO_2 were integrated in the ranges of 1300–2000 cm^{-1} (O—H stretching vibration), 1500–1750 cm^{-1} (N=O stretching vibration) and 2200–2450 cm^{-1} (C=O stretching vibration) respectively, and used as relative measures of H_2O , N_2O and CO_2 contents in the exhaust gases. Where nitrate is present, the traces were deconvoluted to extract H_2O and NO_2 independently.

2.2.4. Attenuated total reflectance Fourier Transform-Infrared

Attenuated total reflectance (ATR) Fourier Transform-Infrared (FT-IR) spectra were recorded in the mid-region on a Bruker Tensor 27 FT-IR spectrometer between 600 and 4000 cm^{-1} with a resolution of 6 cm^{-1} by transmittance on small amounts of powder. Spectra were background corrected and scaled to ease comparison: on the 1520–1700 cm^{-1} (H—O—H bending) and 3400–4000 cm^{-1} (O—H stretching vibration) from the water loss quantify by TGA between 30 and 250 °C to ease comparison.

2.2.5. ^{27}Al magic-angle spinning (MAS) solid state nuclear magnetic resonance (NMR)

Solid state ^{27}Al MAS NMR spectra were measured using a 2.5 mm CP/MAS probe on a Bruker Avance III NMR spectrometer. The ^{27}Al MAS NMR single pulse experiments were recorded at 104.3 MHz applying the following parameters: 25'000 Hz sample rotation rate, between 2000 and 4000 scans depending of the content of aluminium in the samples, $\pi/2$ pulses of 1.5 μs , 0.5 s relaxation delays (identical spectra were obtained when relaxation delays of 0.2, 0.5 & 1.0 s were applied), without ^1H decoupling. The ^{27}Al NMR chemical shifts of the were referenced to an external sample of $\text{Al}(\text{acac})_3$. The ^{27}Al MAS NMR spectra were analysed by the line shape fitting software “DMFIT” [26]. Generally, the fitting of the octahedral sites was performed using i) a Lorentzian shape at 9 ppm (line widths of ca. 270–450 Hz) and ii) a quadrupolar broadened shape using the “Czjzek simple” [27] as detailed in [20].

2.2.6. Energy dispersive spectrometry (EDS)

The semi-quantification of Mg, Al, Cl, S was done with Zeiss Sigma 500 VP FE-SEM with Oxford Instruments Aztec Energy Advanced Xmax 150 EDS detector. The working distance used for the point analysis was 8.5 mm. To avoid charging artefacts, the powder samples were carbon coated using an evaporative coater. The EDS measurements were calibrated by measuring Co and 50 points were recorded for each sample.

2.3. Analysis of the solutions

After the collection of each syringe sample, the pH was measured in a 50 μL aliquot with a Thermo Scientific™ Orion™ PerpHec™ ROSS™ Combination pH Micro Electrode, and the rest of the sample was kept in refrigerator until further analysis.

Total dissolved inorganic carbon (TIC) was determined by infrared spectrometric techniques using an Analytic Jena Multi N/C 2100S equipped with an infrared NDIR-detector and an APG autosampler and supported by the Software multiWin (aj). TIC is determined directly by oxidation of the dissolved inorganic to CO_2 using 10% phosphoric acid, which is diluted from 85% phosphoric acid (p.a., Merck), injecting the released CO_2 with synthetic air and analysing with the NDIR infrared detector.

The samples were analysed for major cations by ICP-OES on a Varian 720 ES equipped with an autosampler Varian SPS-3 supported by the ICP Expert II Ver. 1.1.2 software and Varian Spectroscopy Database Administrator Ver. 1.6.0.20. Solution samples were diluted with 1% HNO_3 by a factor of 100 before injection. The samples were analysed for the anions (chloride, nitrate, sulphate) by ion chromatography using a Metrohm ProflC AnCat MCS IC system with automated 5 μL and 50 μL injection loops.

2.4. Thermodynamic calculations

The solubility products were calculated from the measured concentrations using the Gibbs free energy minimization software GEMS [28]. GEMS is a broad-purpose geochemical modelling package that computes

Table 1

Standard thermodynamic properties (25 °C) and molar volumes of the phases considered in this study with indication of references; some of them are summarized in [21] and directly available in the cemdata18 database, others are estimated from the literature available and ion-exchange constant measured by [14] on hydrotalcite with Mg/Al = 2.35.

	logK _{so} ^a given	Log K _{so} (re) calculated ^b	Δ _f G° (Gibbs free energy of formation) [kJ/mol]	V° (molar volume) [cm ³ /mol]	S° [J/ mol/K]	Cp° [J/mol/ K]	Ref.
MgCO ₃			-1029.5	28.0	65.7	81.0	[29,33]
MgCl ₂			-591.8	40.1	89.6	90.8	[29,33]
Mg(NO ₃) ₂			-589.2	62.9	164.0	119.2	[29,33]
MgSO ₄			-1170.5	42.8	91.4	95.7	[29,33,34]
Brucite Mg(OH) ₂	-11.16		-832.23	24.6	63.1	77.3	[29,33]
Microcryst. Al(OH) ₃	-0.67		-1148.40	32.0	140	93.1	[30]
H ₂ O (zeolitic water)			-237.183	18.1	69.9	75.4	[21,33]
OH-hydrotalcite							
OH-hydrotalcite 2:1 Mg ₄ Al ₂ (OH) ₁₄ ·3H ₂ O	-56.02		-6394.56	219	548.9	648.6	[5,21]
OH-hydrotalcite 2:1 Mg ₄ Al ₂ (OH) ₁₄ ·3H ₂ O	-49.70		-6358.49	219	548.9	647.6	[7] [21] re-calculated from experimental values from [31]
OH-hydrotalcite 2:1 Mg ₄ Al ₂ (OH) ₁₄ ·3H ₂ O	-54.51		-6407.26	227	513.0	556.2	[35]
OH-hydrotalcite 3:1 Mg ₆ Al ₂ (OH) ₁₈ ·5H ₂ O	-72.0		-8022.9	305	675.2	803.1	[7] [21] re-calculated from experimental values from [31]
OH-hydrotalcite 4:1 Mg ₈ Al ₂ (OH) ₂₂ ·3H ₂ O	-94.34		-9687.40	392	801.4	957.7	[7] [21] re-calculated from experimental values from [31]
OH-hydrotalcite 2.35:1 ^b Mg _{4.7} Al ₂ (OH) _{15.4} ·3H ₂ O		-63.83 ^b	-6977.11	175			Calculated based on value given in [5]
OH-hydrotalcite 1.9:1 Mg _{3.85} Al ₂ (OH) _{13.7} ·3.32H ₂ O	-31.59 ^c	-45.07 ^d	-6215.72 ^d	235	615.4	733.9	[24], recalculated
OH-hydrotalcite 2.9:1 Mg _{5.79} Al ₂ (OH) _{17.57} ·4.89H ₂ O	-46.33 ^c	-67.33 ^d	-8162.14 ^d	301	847.3	1001.7	[24], recalculated
CO ₃ -hydrotalcite							
CO ₃ -hydrotalcite 2:1 Mg ₄ Al ₂ (OH) ₁₂ (CO ₃)· 2H ₂ O	-51.14		-6342.97	221			[5,36]
CO ₃ -hydrotalcite 2:1 Mg ₄ Al ₂ (OH) ₁₂ (CO ₃)· 2H ₂ O	-58.23		-6354.3	231	552.1	604.2	[35]
CO ₃ -hydrotalcite 2:1 Mg ₄ Al ₂ (OH) ₁₂ (CO ₃)· 5H ₂ O	-44.19		-6777.66	221	626.7	795.3	[13]
CO ₃ -hydrotalcite 2:1 Mg ₄ Al ₂ (OH) ₁₂ (CO ₃)· 4H ₂ O	-52.40		-6825.10	219	587.8	685.8	[22,23]
CO ₃ -hydrotalcite 3:1 Mg ₆ Al ₂ (OH) ₁₆ (CO ₃)· 5H ₂ O	-66.58		-8679.70	230	822.9	1025.2	End member in [12]
CO ₃ -hydrotalcite 3:1 Mg ₆ Al ₂ (OH) ₁₆ (CO ₃)· 5H ₂ O	-74.82		-8726.73	305 ^e	750.3	879.8	[22,23]
CO ₃ -hydrotalcite 4:1 Mg ₈ Al ₂ (OH) ₂₀ (CO ₃)· 6H ₂ O	-97.14		-10,628.37	392	912.7	1073.9	[22,23]
CO ₃ -hydrotalcite 2.35:1 Mg _{4.7} Al ₂ (OH) _{13.4} (CO ₃)·3H ₂ O		-66.64 ^e	-7206.59	178			Additivity based on [14]
CO ₃ -hydrotalcite 1.9:1 Mg _{3.85} Al _{2.02} (OH) _{11.49} (CO ₃) _{1.14} ·3.32H ₂ O	-31.99 ^c	-42.39 ^d	-6542.34 ^d	229	641.6	752.6	[24], recalculated
CO ₃ -hydrotalcite 2.9:1 Mg _{5.79} Al _{1.97} (OH) _{15.44} (CO ₃) _{1.02} ·4.38H ₂ O	-48.36 ^c	-65.09 ^d	-8234.80 ^d	299	816.1	958.7	[24], recalculated
NO ₃ -hydrotalcite							
NO ₃ -hydrotalcite 2:1 Mg ₄ Al ₂ (OH) ₁₂ (NO ₃) ₂	-52.7						[37]
NO ₃ -hydrotalcite 2.35:1 Mg _{4.7} Al ₂ (OH) _{13.4} (NO ₃) ₂ ·3H ₂ O		-54.37 ^e	-6830.38	242			Additivity based on [14]
Cl-hydrotalcite							
Cl-hydrotalcite 2.35:1 Mg _{4.7} Al ₂ (OH) _{13.4} (Cl) ₂ ·3H ₂ O		-56.12 ^e	-6881.14	219			Additivity based on [14]
Cl-hydrotalcite 3:1 Mg ₆ Al ₂ (OH) ₁₆ (Cl) ₂		-69 ^f	-7242.19 ^f				[38]
SO ₄ -hydrotalcite							
SO ₄ -hydrotalcite 1.9:1 Mg _{3.85} Al _{2.05} (OH) _{12.09} (SO ₄) _{0.88} ·3.14H ₂ O	-31.67 ^c	-43.64 ^d	-6606.70 ^d	232	611.6	722.9	[24], recalculated
SO ₄ -hydrotalcite 2.9:1 Mg _{5.79} Al _{2.13} (OH) _{16.08} (SO ₄) _{0.94} ·5.04H ₂ O	-47.49 ^c	-65.89 ^d	-8755.94 ^d	260	872.9	1023.4	[24], recalculated

^a All solubility products refer to the solubility with respect to the species Mg²⁺, Al(OH)₄⁻, OH⁻, CO₃²⁻, NO₃⁻, Cl⁻, SO₄²⁻ or H₂O.

^b Calculated using the additivity method, based on the value given in [5], composition corresponds to Mg/Al reported in [14].

^c Values given in (Prentice et al., 2020).

^d Recalculated using the reported concentrations, with the exception of Mg, where [Mg] at equilibrium with brucite was considered, as measured Mg concentrations were more than 10 times higher, indicating analytical problems.

^e Calculated from additivity based on [14] and OH-hydrotalcite with Mg/Al = 2.35.

^f Log K calculated from Δ_rG° given in [38].

equilibrium phase assemblage and speciation in a complex chemical system from its total bulk elemental composition. The thermodynamic data for aqueous species and for brucite ($\text{Mg}(\text{OH})_2$) were taken from the GEMS version of the PSI/Nagra thermodynamic database [29], data for microcrystalline aluminium hydroxide (microcrystalline $\text{Al}(\text{OH})_3$) from [21,30], as summarized in Table 1.

Due to the variable composition of hydrotalcite, only few thermodynamic data are available and vary strongly between different studies. The data found in literature are summarized in Table 1. While [5] derived a very stable $\text{Mg}_4\text{Al}_2(\text{OH})_{14}\cdot 3\text{H}_2\text{O}$ ($\log K_{s0} = -56.0$), Myers et al. [7] used measured concentrations from short term experiments of a few hours (up to 12 h) [31] to calculate the solubility product for three hydroxide based end-members for MA-OH-LDH $\text{Mg}_4\text{Al}_2(\text{OH})_{14}\cdot 3\text{H}_2\text{O}$ ($\log K_{s0} = -49.70$), $\text{Mg}_6\text{Al}_2(\text{OH})_{18}\cdot 3\text{H}_2\text{O}$ ($\log K_{s0} = -72.02$) and $\text{Mg}_8\text{Al}_2(\text{OH})_{22}\cdot 3\text{H}_2\text{O}$ ($\log K_{s0} = -94.34$). Recently, [22,23] estimated thermodynamic data for carbonated MA-c-LDH phases: $\text{Mg}_4\text{Al}_2(\text{OH})_{12}(\text{CO}_3)\cdot 4\text{H}_2\text{O}$ ($\log K_{s0} = -52.40$), $\text{Mg}_6\text{Al}_2(\text{OH})_{16}(\text{CO}_3)\cdot 5\text{H}_2\text{O}$ ($\log K_{s0} = -74.82$), and $\text{Mg}_8\text{Al}_2(\text{OH})_{20}(\text{CO}_3)\cdot 6\text{H}_2\text{O}$ ($\log K_{s0} = -97.14$) from the results of [14] using the additivity method [32], which are several log units more stable than the data reported by [13]. Table 1 also contains data derived here from additivity methods from [14]. A recent publication from Prentice et al. [24] gave thermodynamic data for hydrotalcite containing carbonate, hydroxide and sulphate and these authors observed a dependence of solubility products on pH. Their calculations involved magnesium concentrations measured well above the brucite solubility; based on their measured concentrations the $\log K_{s0}$ were recalculated assuming magnesium concentrations at equilibrium with brucite and these are given in Table 1.

The thermodynamic data between 5 and 100 °C at 1 bar were obtained based on the temperature dependence of the apparent Gibbs free energy of formation:

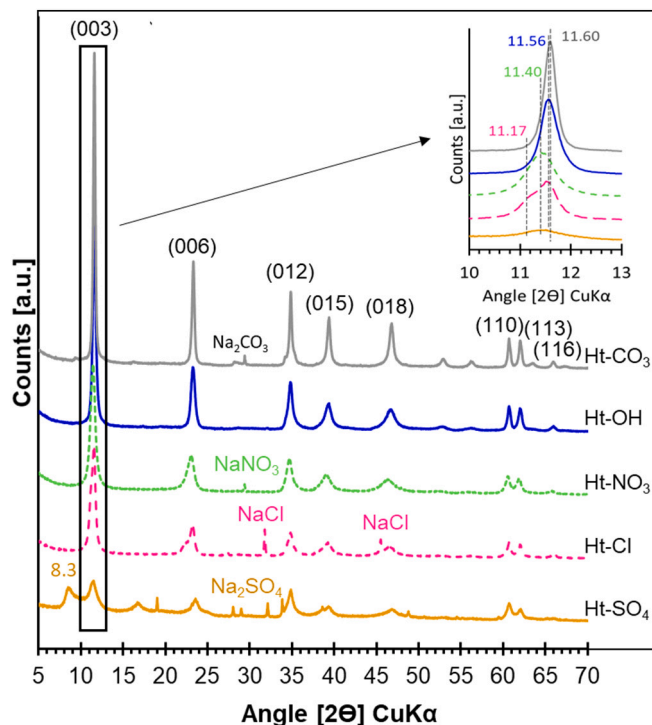


Fig. 2. X-ray diffraction (XRD) patterns of 80 °C-synthesised hydrotalcites.

Richardson gathering numerous Mg-Al layered double hydroxide crystal structure [11] derived linear relationship between the cell parameter a and the $\text{Al}/(\text{Mg} + \text{Al})$ in the hydrotalcite's crystal structure.

$$\Delta_a G_T^o = \Delta_f G_{T_0}^o - S_{T_0}^o (T - T_0) - \int_{T_0}^T \int_{T_0}^T \frac{C_p^o}{T} dT dT = \Delta_f G_{T_0}^o - S_{T_0}^o (T - T_0) - a_0 \left(T \ln \frac{T}{T_0} - T + T_0 \right) - 0.5a_1 (T - T_0)^2 - a_2 \frac{(T - T_0)^2}{2T \cdot T_0^2} - a_3 \frac{2(\sqrt{T} - \sqrt{T_0})^2}{\sqrt{T_0}} \quad (2)$$

where a_0 , a_1 , a_2 , and a_3 designate the empirical coefficients of the heat capacity equation $C_p^o = a_0 + a_1 T + a_2 T^2 + a_3 T^{-0.5}$ and T_0 the reference temperature of 298.15 K, see [39] and the online documentation of GEMS by Kulik [40]. The apparent Gibbs free energy of formation $\Delta_a G_{T_0}^o$ refers to the Gibbs free energies of the elements at 298 K, and Eq. (2) is built into the GEMS code.

3. Results and discussions

3.1. Solid characterisation of hydrotalcite synthesised at 80 °C

The XRD data of the hydrotalcite samples (i.e. Ht- CO_3 , Ht-Cl, Ht- SO_4 , Ht- NO_3 , Ht-OH) synthesised at 80 °C are shown in Fig. 2; the main reflection peaks of hydrotalcite are indexed in Table 2 based on [41]. The reflections characteristic of the hydrotalcite at 11.5 ± 0.3 (0 0 3), 23.3 ± 0.3 (0 0 6), 34.8 ± 0.3 (0 1 2), 39.0 ± 0.3 (0 1 5), 46.9 ± 0.3 (0 1 8), 60.7 ± 0.3 (1 1 0), 62.1 ± 0.3 (1 1 3) and 66.1 ± 0.3 2 θ (1 1 6) are observed confirming the formation of hydrotalcite in all samples, while no crystalline $\text{Mg}(\text{OH})_2$ or $\text{Al}(\text{OH})_3$ phases were detected. Some residual sodium-based salts from the synthesis were still present in the samples. Note that the basal distance or cell parameter c of the hydrotalcite crystal structure does not depend on Mg/Al ratios but on the anions present in the interlayer. The cell parameter a (average metal-metal distance in the brucite-like layer) calculated from the (1 1 0) position, slightly increases (0.02 Å) when increasing the Mg/Al from 2 to 3 [42].

While the reflection peaks are well defined for the Ht- CO_3 , broader and asymmetrical peaks related to the basal plane were observed in the other samples indicate smaller crystallites or less ordered structures. The broadness of these peaks increased depending on the anion incorporated: $\text{OH}^- < \text{NO}_3^- < \text{Cl}^- < \text{SO}_4^{2-}$. In agreement with our observations, literature reports an increase of the basal spacing together with a broadening of the peak compared to CO_3 -hydrotalcite, when Cl^- , NO_3^- and SO_4^{2-} is present in the interlayer of hydrotalcite [43,44].

The SSA was calculated from the nitrogen sorption and the results are given in Table S2. The values were between 18 and 33 m^2g^{-1} and no increase with the broadening of the reflection peaks in the XRD patterns was observed. The broadening of the reflection peaks is therefore rather linked to crystallinity of the phases than to their size.

The drying procedure can potentially affect the measured (0 0 l) distance, as strong drying can remove water present in the interlayer. However, although the Ht- CO_3 sample had been freeze-dried before analysis, it showed the same sharp (0 0 3) reflection corresponding to a basal spacing of 7.63 Å which is characteristic of common carbonated hydrotalcite, e.g. [43,45,46] as the Ht- CO_3^* samples, indicating little effect of the freeze drying on the basal spacing. The basal spacing of the Ht-OH sample was measured at about 7.65 Å which is within or slightly higher than the range of previously reported values 7.55–7.67 Å [24,43]. This could be due to a small carbonation contamination (see below, TGA data).

The (0 0 3) reflection of the other hydrotalcite samples (Ht-Cl, Ht-

Table 2
Indexing of X-ray diffraction pattern, spacing and intensities for hydrotalcite samples.

h	k	l	Ht - CO ₃ [*]				Ht - OH				Ht - NO ₃				Ht - Cl				Ht - SO ₄			
			2θ[°]	d[Å]	I[%]	comment	2θ[°]	d[Å]	I[%]	comment	2θ[°]	d[Å]	I[%]	comment	2θ[°]	d[Å]	I[%]	comment	2θ[°]	d[Å]	I[%]	comment
0	0	3*									11.28	7.84	46.6		11.16	7.93	37.3		8.30	10.39	48.8	
0	0	3	11.60	7.63	100.0		11.52	7.68	100.0		11.40	7.76	53.4		11.56	7.65	62.7		11.42	7.75	51.2	
0	0	6*																	16.64	5.33	18.3	
0	0	6*																	19.03	4.66		Na ₂ SO ₄
0	0	6*	23.33	3.81	26.1	23.33	3.81	33.3			23.13	3.85	14.7		22.24	4.00	6.5		23.67	3.76	37.2	
0	0	6**													23.27	3.82	18.1		24.71	3.60	9.9	
0	0	6**									29.39	3.04		NaNO ₃					28.04	3.18		Na ₂ SO ₄
0	1	2	34.81	2.58	7.9	34.17	2.62	2.8			34.75	2.58	14.0		34.78	2.58	13.4		29.00	3.08		Na ₂ SO ₄
0	1	5	39.36	2.29	5.1	39.32	2.29	14.8			39.02	2.31	7.6		39.37	2.29	7.6		32.14	2.79		Na ₂ SO ₄
0	1	8	46.78	1.94	4.6	46.84	1.94	13.5			46.60	1.95	5.4		45.50	1.99	10.1	NaCl	33.85	2.65		Na ₂ SO ₄
0	1	-10	52.95	1.73	0.9	52.97	1.73	2.5			52.31	1.75	0.7	Traces	46.31	1.96	5.0		34.82	2.58	47.1	
0	1	11	56.21	1.64	0.6	56.19	1.64	1.8			55.68	1.65	0.6	Traces					39.36	2.29	18.5	
1	1	0	60.69	1.53	4.2	60.70	1.52	9.2			60.52	1.53	7.4		60.72	1.53	8.9		60.71	1.53	29.2	
1	1	3	62.03	1.50	4.1	62.06	1.49	8.4			61.85	1.50	6.4		62.05	1.50	7.5		62.09	1.49	18.4	
0	1	-13	63.42	1.47	0.5	63.63	1.46	1.4		Traces												
1	1	6	65.92	1.42	1.0	65.96	1.42	1.9			65.78	1.42	1.3		65.92	1.42	1.4		65.99	1.42	3.6	
V _{cell}						185 Å					189 Å				184 Å				193 Å/252 Å			

NO₃ and Ht-SO₄) is split in two signals: a first signal relatively constant at $d \approx 7.65$ Å (11.56 2°Θ, see Table 2) for Ht-Cl and at $d \approx 7.75$ Å (11.41 2°Θ) for Ht-NO₃ and Ht-SO₄. And a second, more intense reflection peak corresponding to a bigger basal spacing at 7.84 Å (11.28 2°Θ), 7.93 Å (11.16 2°Θ) and 10.39 Å (8.30 2°Θ) for Ht-Cl, Ht-NO₃ and Ht-SO₄, respectively. In the case of Ht-SO₄ the split results in two distinct peaks. The occurrence of two peaks was observed in previous studies [44] and is most likely related to carbonate impurities as observed by TGA (as discussed further below).

In the case of Ht-Cl the second basal spacing of the first reflection agrees with literature (e.g., [43]). The basal spacing for Ht-NO₃ is lower than previously reported values of 8.1–8.8 Å (e.g., [14,47]). This could be related to the harsher drying used, which removed some water from the interlayer and hence, reduced the basal spacing. Another possibility is presence of CO₃²⁻ impurities in the interlayer of NO₃⁻ hydrotalcite, which would cause a smaller basal spacing as the CO₃²⁻ size is smaller than the one of NO₃⁻.

For sample Ht-SO₄, the first peak at 10.39 Å (8.30 2Θ) was above and the second peak at 7.75 Å (11.41 2Θ) below the numbers found in literature as 8.6–8.9 Å [43,44]. This indicates a segregation due to the presence of sulphate and carbonate anions (from impurities) in the interlayers. The first 003 peak at 10.39 Å (8.30 2Θ) contains mostly the SO₄²⁻ anions layers, as LDH-sulphates with a basal spacing of up to 11 Å have been observed due to the swelling of the interlayers by water [43]. This is supported by the observation of excess water observed by TGA for this sample (see below) and the rapid collapse of the first peak during in situ temperature XRD (see Section 3.2). The second 003-peak at 7.75 Å (11.41 2Θ) contains mostly CO₃²⁻ anions as impurity and a small amount of SO₄²⁻, hence the basal spacing is drastically smaller.

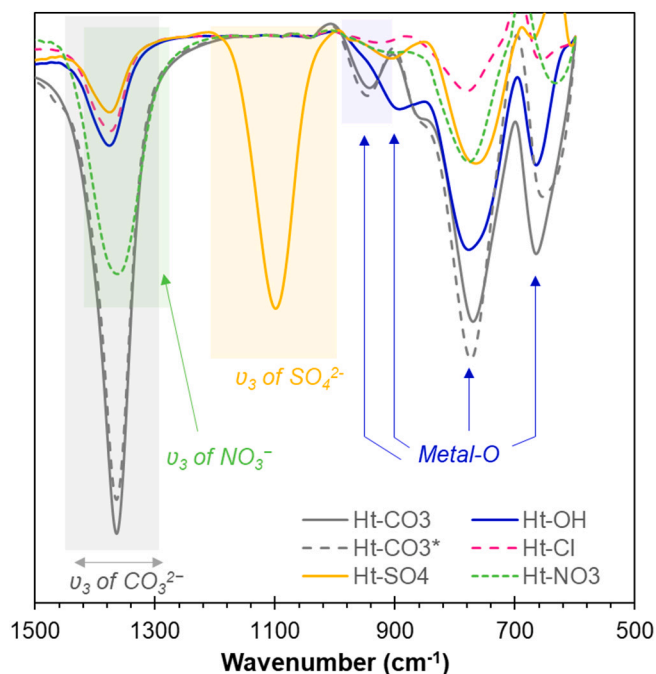
The estimated cell volumes of the hydrotalcite samples are presented in Table 2. The cell volumes of the Ht-CO₃, Ht-OH and Ht-Cl samples were between 184 and 186 Å³ despite the different anion size and structure. This indicates a low effect of the incorporated anion on the structure: Cl⁻ \approx CO₃²⁻ \approx OH⁻. The estimated cell volume for Ht-NO₃ was about 189 Å³, while the split reflection peak presented by the Ht-SO₄ lead to two estimated cell volumes of 188 (corresponding to the presence of carbonate) and 252 Å³ corresponding to the sulphate-hydrotalcite. The cell volume of the hydrotalcite sample increases with the size of the incorporated anion Cl⁻ \approx CO₃²⁻ \approx OH⁻ < NO₃⁻ < SO₄²⁻.

The FT-IR spectra of hydrotalcite samples measured between 600 and 4000 cm⁻¹ are shown in Fig. S1; a zoom of the range 600–1500 cm⁻¹ is presented in Fig. 3. The characteristic bands of the hydroxyl groups between 2600 and 4000 cm⁻¹ (O–H stretching) and of free water between 1625 and 1650 cm⁻¹ (O–H bending of water) were found in all the samples. The broad and mixed bands characteristic of the hydroxyl groups were more defined for the Ht-CO₃ and Ht-OH samples with the detection of shoulders at 3100 cm⁻¹, while the band areas were broader in the Ht-Cl, Ht-NO₃, and Ht-SO₄ samples confirming smaller crystallite or less ordered structure for the Ht-Cl, Ht-NO₃, and Ht-SO₄ samples. Carbonates were also found in all the samples as visible by the asymmetric stretching of CO₃²⁻ in the range 1400–1500 cm⁻¹ [48], indicating a carbonate contamination, although limited, in all the samples. The asymmetric stretching of NO₃⁻ is in a similar range as the CO₃²⁻ band and overlaps [49,50]. Finally, the M–O bands (where M=Al or Mg) between 660 and 950 cm⁻¹ were more defined for the Ht-CO₃ and Ht-OH samples and can be related to a better crystallinity as observed in the XRD data.

The ²⁷Al MAS NMR spectra of the hydrotalcite samples are shown in Fig. 4. The ²⁷Al MAS NMR spectra showed a sharp resonance at 9–11 ppm corresponding to an Al(VI) signal, confirming the predominant presence of aluminium in octahedral sites of the hydrotalcite. In addition a weak signal at 70–80 ppm indicating the presence of some Al(IV) was observed. The later was assigned to the presence of a low amount of asymmetric dehydroxylated Al(IV) in hydrotalcite [46]. The ²⁷Al NMR chemical shift of the Al(IV) environment depends on the composition of

Table 3Compositions and quadrupolar parameters of Al (IV) and Al(VI) sites determined by line shape simulation of ^{27}Al MAS NMR data from Fig. 4.

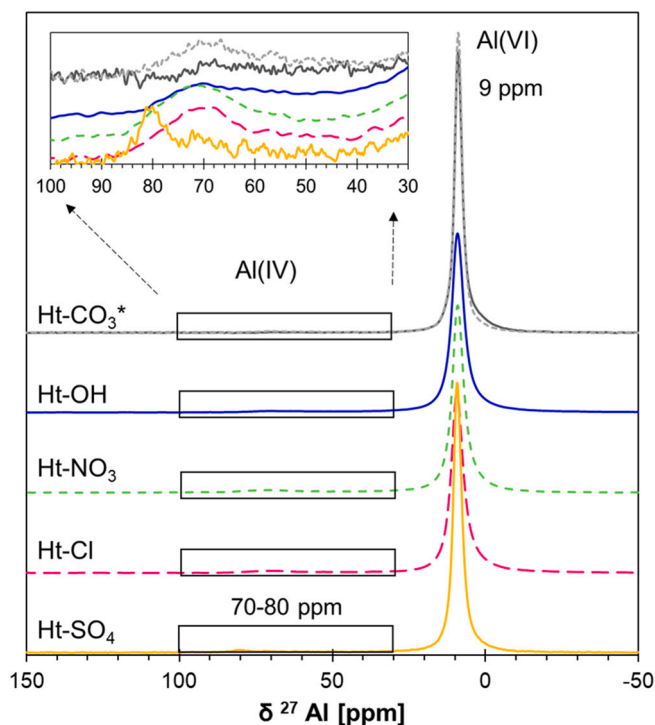
	Asymmetric Al(IV)		Asymmetric Al(VI)		Symmetric Al(VI)	
	δ_{iso}	Rel. amount	δ_{iso}	Rel. amount	δ_{iso}	Rel. amount
	[ppm]	[%]	[ppm]	[%]	[ppm]	[%]
Ht-CO ₃ *	79.0	1			8.9	99
Ht-CO ₃			10.2	12	9.0	88
Ht-Cl	77.9	3	10.6	11	9.4	86
Ht-NO ₃	80.3	4	10.4	9	9.1	86
Ht-SO ₄	85.5	2	10.2	12	9.3	86
Ht-OH	77.6	2	10.6	7	8.9	86

**Fig. 3.** FT-IR spectra of the hydrotalcite samples zoomed between 600 and 1500 cm^{-1} , full spectra are given in Fig. S1.

the cations present on the surface to compensate for the negative charge [51]. The large variation from 78 ppm for Ht-Cl to 86 ppm for Ht-SO₄ seems to be related to the presence of different anion in the vicinity of the Al(IV).

The ^{27}Al MAS NMR spectra were deconvoluted as detailed in [20] for hydrotalcite; the weak Al(IV) signal was deconvoluted using an asymmetric shape and quantified between 1 and 4% of the total aluminium in the solids. The main Al(VI) signal is better fitted with a symmetric signal at 9.1 ± 0.3 ppm and a second asymmetric signal at 10–11 ppm. The commercial Ht-CO₃* sample contained only the symmetric Al(VI) signal, while the re-precipitated samples contained about $10\% \pm 3\%$ of asymmetric Al(VI). This asymmetric Al(VI) resonance might indicate a less crystalline structure. Alternatively, this asymmetric Al(VI) may also indicate the presence of poorly aluminium hydroxide gels [52] although not detected by XRD or TGA. Therefore, the aluminium is considered to be only incorporated in hydrotalcite.

The ^{23}Na MAS NMR spectra associated to the hydrotalcite samples are shown in Fig. S2 in SI and for each hydrotalcite one signal was observed with a different shift. Signals at 7.4, 1.1, 0.0 and -8.0 ppm in the ^{23}Na MAS NMR spectra were present for Ht-Cl, Ht-CO₃, Ht-SO₄ and Ht-NO₃ samples corresponding to the resonance of NaCl, Na₂CO₃, Na₂SO₄ and NaNO₃ [53,54], respectively. Sodium is neither expected to precipitate within the hydrotalcite structure nor to be sorbed on the positively charged main layers. However, the presence of weak broad

**Fig. 4.** ^{27}Al MAS NMR spectra (scaled to ease the comparison) of hydrotalcite samples (dashed line corresponds to the initial hydrotalcite-CO₃ from Sigma Aldrich). The mean centers of gravity of specific regions are given and the mean isotropic ^{27}Al MAS NMR chemical shifts are given in Table 3.

signal at -4.6 ppm in the Ht-OH's spectrum indicated the presence of some hydrated NaOH [54] supposedly taken up in the interlayer or near the outer surface.

The thermogravimetric analyses (TGA) of the Ht-CO₃ and Ht-CO₃* samples are presented in Fig. 5a, the TGA of the other samples are shown in Fig. 5b and a summary of the weight losses are detailed in Table 4. Two loss regions at 30–320 °C and 320–600 °C characteristic for hydrotalcite can be seen [24] related the first loss region between 30 °C and 270 °C to physically and chemically bound water and the second to the interlayer anion. We attributed the first weight loss to water loss, water present as both physical water and as interlayer water and the second peak to the main layer water and water associated with the anion. Similar water losses are commonly observed for calcium aluminium based LDH, so called AFm phases [55].

The Ht-SO₄ sample started to loose water from the beginning of the heating process, indicating a remaining excess of water in agreements with the large basal spacing of 11.39 Å observed by XRD. Although this could also be related to the dehydration of hydrated Na₂SO₄ impurities remained in the sample. The Ht-Cl samples also started to loose water below 80 °C, while the Ht-CO₃, Ht-OH and Ht-NO₃ started to loose water around 80 °C.

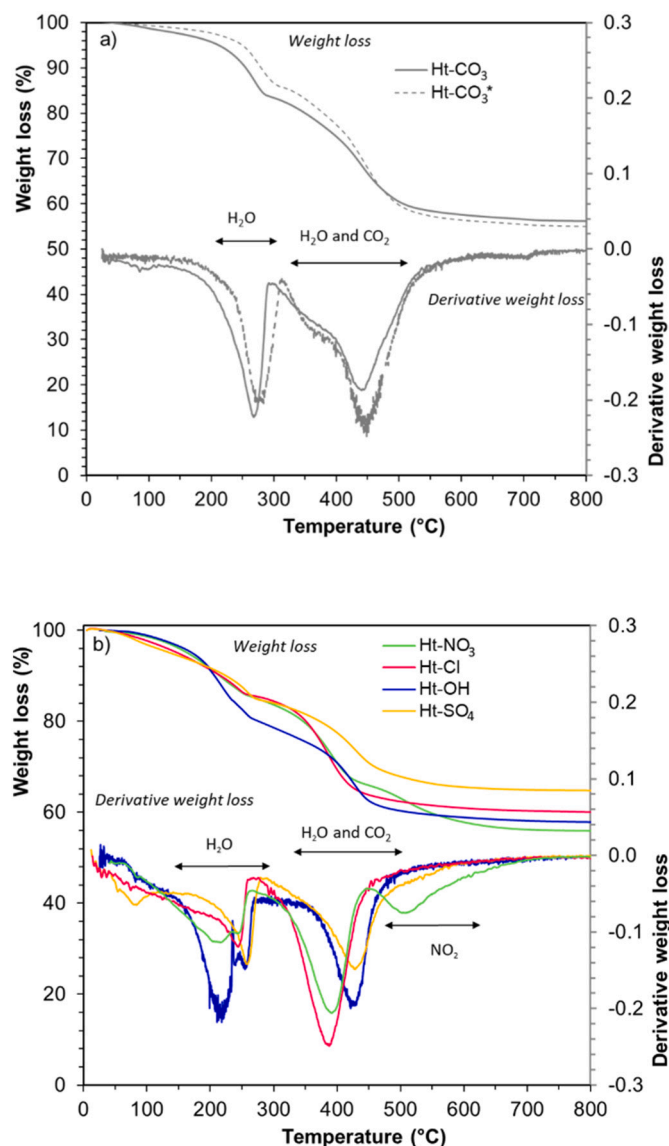


Fig. 5. Thermogravimetric analysis (TGA) and derivative of the TGA for a) the Ht- CO_3^* and the Ht- CO_3 samples, b) the Ht- NO_3 , Ht-Cl, Ht- SO_4 and Ht-OH samples.

The FT-IR analysis of the exhausted gas of the TGA was used to understand the nature of the second and third weight loss for the Ht- CO_3^* , Ht- CO_3 , Ht-OH and Ht- NO_3 samples. The deconvolutions of the TGA-FT-IR are presented in the SI. The Ht- CO_3^* sample was used to quantify the trace of H_2O and CO_2 in other samples, i.e. the traces were normalised based on the traces obtained for the reference sample. The water loss occurred over a large range from 30 to 600 °C, with carbonates were observed between 400 °C–650 °C, as summarized in Table 5. The theoretical 1 carbonate per 2 Al in hydrotalcite with $\text{Mg}/\text{Al} = 2$ was found by the analysis of the TGA data of the Ht- CO_3 sample. Also the other samples contained some CO_2 (see SI) confirming the FT-IR data of

the solids: 0.2, 0.4, 0.3 and 0.35 CO_3^{2-} per 2Al in formula unit were calculated in the Ht-OH, Ht-Cl, Ht- SO_4 and Ht- NO_3 samples, respectively.

For Ht- NO_3 , NO_2 was lost between 400 °C and 650 °C arising from nitrate salt decomposition slightly above a temperature observed by [56], who reported a loss starting at 280 °C, but similar to the temperature observed by [44]. 1.1 NO_3^- per 2Al in formula unit were calculated in the Ht- NO_3 .

Cl_2 was released progressively between 400 and 1000 °C, which corresponds to data reported in literature [44]. SO_2 seemed to be exhausted starting from 500 °C, differently from literature where [44] reported that sulphate grafted the oxide layers with the increase of temperature and stayed in the structure until SO_2 was released starting at 800 °C. Thus, the contents of Cl^- and SO_4^{2-} were not determined by this method. The content of hydroxyl group in each sample was obtained from the charge balance after taking into account the content of the other anions and then the water molecules were calculated from the left over from the total water loss.

Based on the TGA results (when possible), the SEM/EDS data and the mass balance (Table S3) from calculation based on starting and final solution concentrations (i.e. considering the fraction of anions remaining in solution, see below), an estimation of the composition is given in Table 5. The TGA, SEM/EDS and the mass balance data agreed within the error margin.

3.2. Anion dependency and thermal stability studied by in-situ heated X-ray powder diffraction

The changes in the water content upon heating can also be followed by the changes of the basal spacing. The evolution of the mean basal spacing obtained by in situ X-ray powder diffraction experiments during heating from 100 to 300 °C are shown in Fig. 6 (a video clip of the 003-peak evolution in SI). Every sample showed a slight reduction (0.1–0.2 Å) of the basal spacing between 100 to ~150 °C. Ht- SO_4 additionally lost its first diffraction peak (at 10.39 Å, left shoulder of the main peak), confirming the excess of water in the sample. At around 150–155 °C the peak of Ht- CO_3 and Ht-OH collapsed rapidly and emerged as a new sharp peak at ~6.6 Å in a rapid transition. In the case of Ht-Cl the main peak remained while a new second peak (at ~7.4 Å) was formed. Ht- SO_4 showed a similar behaviour although its basal spacing was reduced by ~0.3 Å. The only sample not forming a second peak was Ht- NO_3 . However, its spacing was also reduced (~0.3 Å) and the peak became increasingly broad. The second peaks of Ht- SO_4 (~7 Å), Ht- CO_3 (~6.5

Table 5

Estimation of the composition of the hydrotalcite samples (adapted from the TGA, EDS data and mass balance results, see Table S3).

	Ht- CO_3	Ht-OH	Ht-Cl	Ht- SO_4	Ht- NO_3
Mg^{2+}	4	4	4	4	4
Al^{3+}	2	2	2	2	2
OH^-	12	13.8	12.7	11.8	12.4
CO_3^{2-}	1	0.1	0.3	0.3	0.3
Cl^-			0.7		
SO_4^{2-}				0.8	
NO_3^-					1
H_2O	4	4	4	4	4

Table 4

Weight losses observed in the TGA curves for the different hydrotalcite samples.

	Below 100 °C	Between 100 and 320 °C	Above 320 °C		
Ht- CO_3			265 °C strong	355 °C shoulder	440 °C strong
Ht-OH		215 °C strong	260 °C shoulder		425 °C strong
Ht-Cl				390 °C strong	
Ht- SO_4	80 °C weak		260 °C strong		425 °C strong
Ht- NO_3		210 °C strong		390 °C strong	

Å), Ht-OH (~ 6.5 Å) and Ht-Cl (~ 7.1 Å) collapsed at ~ 240 – 255 °C followed by the main peak of Ht-Cl shortly afterwards. The third and final peak of Ht-SO₄ (at ~ 6.6 Å) remained even to 300 °C, although it became a broad and small hump at the very end. A similarity of all samples is the slight increase of the basal spacing towards the end of their existence, mainly from the broadening of the main diffraction peak. The main difference is mostly related to the dehydration shown by the TGA (Fig. 5). The dehydration of Ht-CO₃ and Ht-OH was a clean transition, due to the evaporation of the interlayer water molecules. Ht-Cl encapsulated in what appears to be an intermediate stage which allows the co-existence of a fully hydrated and dehydrated phase. However, Ht-Cl had no continuous shift to the second 003 peak as one would expect, rather the hydrated peak is barely outlasting the dehydrated one (which can also be observed in the full pattern XRD measurement). One proposed explanation is the existence of a strong electrostatic interaction between the layers of high charge density and the anion because the interlayer distance (2.88 Å) is smaller than the anion itself ($\text{Cl}^- = 3.62$ Å). Hence, the basal spacing remains unaffected by the release of water molecules [43]. However, it is unclear why this effect does not occur in the other samples as their basal spacing is also smaller than their anion. The occurrence of the second peak might then be explained by the CO_3^{2-} impurities (Table 5) which form their own anion layer or mix only partially [57] and thus dehydrate more like Ht-CO₃. The evolution of the 003 peak in Ht-NO₃ is similar although a second peak is only observed in the full pattern XRD measurement (see SI) which is in accordance with previous observations [47]. This indicates that the structure of Ht-NO₃ requires more time to form. Peaks of Ht-NO₃ and Ht-Cl become increasingly broad which may indicate differences in the atomic arrangement in the interlayer region, possibly related to the incorporation of CO_3^{2-} (Table 5). Finally, the behaviour of the peak evolution of the Ht-SO₄ samples was similar to the ones of Ht-OH and Ht-CO₃ samples apart from its broader peaks due to its poor crystallinity. The first peak (~ 8.5 Å) that collapsed at ~ 150 °C and was interpreted as already reduced from the 10.39 Å peak measured under ambient conditions. The major difference is the persistence of this peak during dehydration despite Ht-SO₄ being thermodynamically less stable than Ht-OH and

Ht-CO₃ (see below, 3.4). This is probably due to the grafted SO_4^{2-} anions which form crosslinks on the adjacent cation layers above 250 °C [43].

3.3. Liquid analysis

The dissolved concentrations and pH values measured in solution after the synthesis of the different hydrotalcites are reported in Table 6. The Al concentration for the Ht-CO₃ is 0.36 mmol/L and increased to 11 mmol/L for the Ht-OH. Al concentrations were even higher for Ht-SO₄, Ht-Cl and Ht-NO₃ with 35, 57 and 67 mmol/L, respectively. All measured Al-concentrations were below the solubility of microcrystalline $\text{Al}(\text{OH})_3$ except for the Ht-NO₃, where the Al concentrations correspond to the solubility of microcrystalline $\text{Al}(\text{OH})_3$ within the measurement error. In each sample, some dissolved CO₃ was measured confirming some carbonate contamination in the samples. The concentrations of the CO_3^{2-} , Cl^- , SO_4^{2-} and NO_3^- were used to calculate its incorporation and the results are given in Table S 3.

3.4. Thermodynamic data

3.4.1. Solubility products

Based on the analysis of the solutions after the syntheses, the “oversaturated” solubility products of the different hydrotalcites were calculated based on the dissolved concentrations and pH values measured in solution, and are given in Table 7 as oversaturated solubility products. The concentrations of Mg were below the detection limit and concentrations were thus estimated from the solubility of brucite at the measured pH values. For each sample, the solubility products ($\log K_{s0}$) were calculated based 1) on theoretical “ideal” formula (maximum uptake, no CO₂ contamination) and 2) based on the estimated “effective” composition (Table 5). All the oversaturated $\log K_{s0}$ were in the range of -44.1 and -52.5 , with the most stable oversaturated $\log K_{s0}$ for the Ht-CO₃ and Ht-OH with -49.9 and -49.7 respectively; followed by Ht-SO₄ > Ht-Cl > Ht-NO₃, where Ht-NO₃ was the least stable. The $\log K_{s0}$ calculated for the effective compositions were lower than the one of the ideal composition indicating that the incorporation of carbonate in the

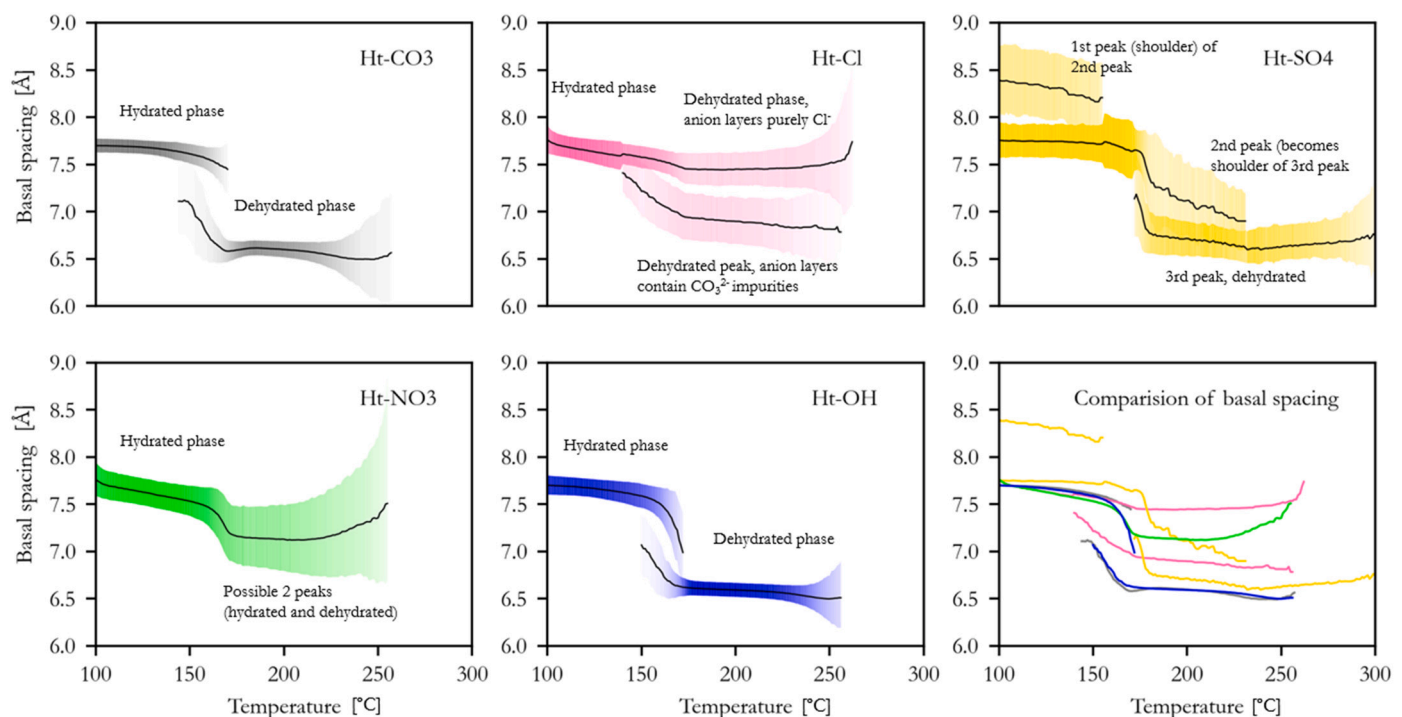


Fig. 6. Mean basal spacing evolution vs. temperature on heating. The peak positions are displayed by the black lines. The peak intensity is displayed by the colour (the more transparent the lower the intensity). The width of the stripes represents the full-width at half maximum (FWHM) of the peaks.

Table 6

Measured concentrations of dissolved species, pH values of solutions after the synthesised hydrotalcite samples at 80 °C. Concentrations given in mmol/L and pH was measured at 22 °C. Note that the Mg concentration were measured in largely diluted aliquots due to the pH and the large amount of Na to preserve the IC device, therefore the detection limit and the dilution give Mg <100 mmol/L.

	[Al]	[CO ₃]	[Cl]	[SO ₄]	[NO ₃]	[Na]	[Mg]	pH
Ht-CO ₃	0.36	294				583	<100	12.9
Ht-OH	11.1	4.29				305	<100	13.8
Ht-Cl	57.1	7.89	1035			1259	<100	13.5
Ht-SO ₄	35.1	8.19		473		1232	<100	13.7
Ht-NO ₃	67.0	7.38			1050	1111	<100	13.2

Table 7

Calculated solubility products of different hydrotalcite compositions at 7, 23, 40 and 80 °C using the effective solid phase composition with the exception of the first line. As the estimated Mg concentration are maximum values, the oversaturation solubility values correspond to an upper limit of the solubility products.

T (°C)	Ht-CO ₃ ^a	Ht-OH ^b	Ht-Cl ^c	Ht-SO ₄ ^d	Ht-NO ₃ ^e
Oversaturated					
23 °C	-49.9 ^f	-49.3 ^f	-46.0 ^f	-47.8 ^f	-44.1 ^f
23 °C	-49.9	-49.7	-47.4	-48.5	-45.4
Undersaturated					
7 °C	-51.7	-49.3	-45.5	-47.1	-45.1
23 °C	-51.8	-49.6	-46.3	-47.0	-46.2
40 °C	-51.6	-48.9	-47.8	-46.3	-47.9
80 °C	-52.5	-47.8	-47.3	-47.7	-49.8
25 °C	-53.0 ± 1.5	-49.9 ± 1.5	-47.0 ± 1.5	-47.8 ± 1.5	-46.6 ± 1.5

^a {Mg²⁺}⁴{AlO₂⁻}²{OH⁻}⁴{CO₃²⁻}¹{H₂O}⁸.

^b {Mg²⁺}⁴{AlO₂⁻}²{OH⁻}^{5.8}{CO₃²⁻}^{0.1}{H₂O}⁸.

^c {Mg²⁺}⁴{AlO₂⁻}²{OH⁻}^{4.7}{Cl⁻}^{0.7}{CO₃²⁻}^{0.3}{H₂O}⁸.

^d {Mg²⁺}⁴{AlO₂⁻}²{OH⁻}^{3.8}{SO₄²⁻}^{0.8}{CO₃²⁻}^{0.3}{H₂O}⁸.

^e {Mg²⁺}⁴{AlO₂⁻}²{OH⁻}^{4.4}{NO₃⁻}¹{CO₃²⁻}^{0.3}{H₂O}⁸.

^f Ideal composition and no CO₂ contamination: {Mg²⁺}⁴{AlO₂⁻}²{OH⁻}⁴{A^{2x}}¹{H₂O}⁸; where x equals to 0.5 for bivalent anions CO₃²⁻ or SO₄²⁻ and to 1 for monovalent OH⁻ or Cl⁻.

structure stabilises the phase, but it did not change the relative order of stability based on the anion type. In literature, carbonated hydrotalcites are also reported as more stable (see Table 1).

A comparison with calcium-aluminium based-LDH (AFm phases) showed a somewhat similar behaviour. The stability of such calcium-aluminium based-LDH is higher for bivalent anions than for monovalent anions, with CO₃-AFm being more stable than SO₄-AFm, followed by NO₃-AFm > Cl-AFm > OH-AFm [21], indicating that not only the charge of the anion but also the structural arrangement of both the anion and the main layer plays an important role in stabilising the different Mg-Al and Ca-Al LDH phases.

The different hydrotalcite samples were re-equilibrated in water at 7, 23, 40 and 80 °C to determine their solubility at different temperatures. After re-equilibration the composition of the solid samples was checked by FT-IR, and in all cases the presence of the added hydrotalcite containing the specific anion was observed as the main solid (see SI, FT-IR). Based on the measured concentrations and the pH values (see SI, Table S4), “undersaturated” solubility products were calculated for the different hydrotalcites based on the effective composition (bold values in Table 7). In most cases, the magnesium concentrations were below the detection limit of 0.002 mmol/L, such that an upper limit for magnesium concentrations was estimated from the solubility of brucite. The results are given in Table 7 and the oversaturated and undersaturated solubility products versus pH are compared in Fig. 7a. The undersaturation data confirmed the sequence observed above, with Ht-CO₃ being the most stable phase, followed by Ht-OH > Ht-SO₄ > Ht-Cl > Ht-NO₃.

Final solubility products at 25 °C were derived taking into account all the undersaturation experiments at the different temperatures (as discussed below), they are summarized in Table 7. These solubility

products were further verified by calculating magnesium and aluminium concentrations as a function of the pH and compared it to the experimental data in Fig. 7b–f. The calculated solubility agrees in all cases well with the measured Al concentration, confirming that the estimated magnesium concentrations were in fact near the brucite solubility line. It is interesting to note that in the case of nitrate and chloride hydrotalcite, the calculated concentrations were only slightly lower than the solubility of brucite and microcrystalline Al(OH)₃, while for OH and carbonate-hydrotalcites much lower Al concentrations were calculated, indicating the Ht-OH and Ht-CO₃ are the most stable hydrotalcites. In general, the solubility products from over and undersaturation agree well, with the exception of Ht-CO₃, where the solubility from oversaturation was 2 to 3 log units higher than the solubility derived from undersaturation, which could indicate a kinetic hindrance. Note, that also the relatively high solubility data (less negative log K_{so} values) from Rozov et al. [12,13] are based on oversaturation experiments.

3.4.2. Effect of temperature on the solubility of hydrotalcite

Fig. 8 shows that the temperature has a minor effect on the solubility of hydrotalcite as the solubility products measured at the different temperatures were comprised within the range of 1–2 log unit for the CO₃, Cl, SO₄ and OH-Ht and 5 log units for the NO₃-Ht. Such a limited effect of temperature has also been observed for Ca-Al-based LDH (AFm phases) containing sulphate, carbonate, chloride, nitrate or hydroxide in the interlayer [21,58].

To describe the solubility at different temperature, entropy and heat capacity values are needed as detailed in Eq. (1). As no entropy or heat capacity data of the different hydrotalcites could be measured, they were estimated i) based on the values of other hydrotalcites and ii) based on their volume as detailed below.

The entropy (S°) of each hydrotalcite was calculated based on the measured entropies given in [59] using the additivity method assuming Δ_rS° ≈ 0 according to Eq. (62) in [32] using Mg(OH)₂ and, MgCl₂, Mg(NO₃)₂, MgSO₄ and MgCO₃ and zeolitic H₂O as constituents as given in [33]. The data are compiled in Table S5. The heat capacity (C_p°) was similarly calculated assuming Δ_rC_p° ≈ 0 following Eq. (78) in Helgeson [32] from the hydrotalcite data given in [59] for each hydrotalcite sample (data presented in Table S5 and Fig. S6).

Recent publications [60,61] highlight the close relationship between the molar volume, V°, the entropy and the heat capacity. Thus, S° was also calculated from the relationship between V° and S° given in [61]. The C_p° was calculated similarly using the averaged linear equation derived for C_p° for hydrotalcite phases in [24]. The additivity and the volume-based values were compared in Table S5 (SI); generally, the values were similar except for the NO₃-Ht and SO₄-Ht. This might due to the approximate values of the entropies of Mg(NO₃)₂ and MgSO₄.

Both the volume and the additivity based data were used to calculate changes of the solubility product with temperature as shown in Fig. 8, where “V°-based” corresponds to the fitting with S° calculated based on the equation given in [61]. For Ht-CO₃, Ht-OH and Ht-Cl the volume based S° and C_p° values or the additivity based data described the observed changes in solubility well, and no further fitting step was conducted. The additivity based data were selected as they rely on

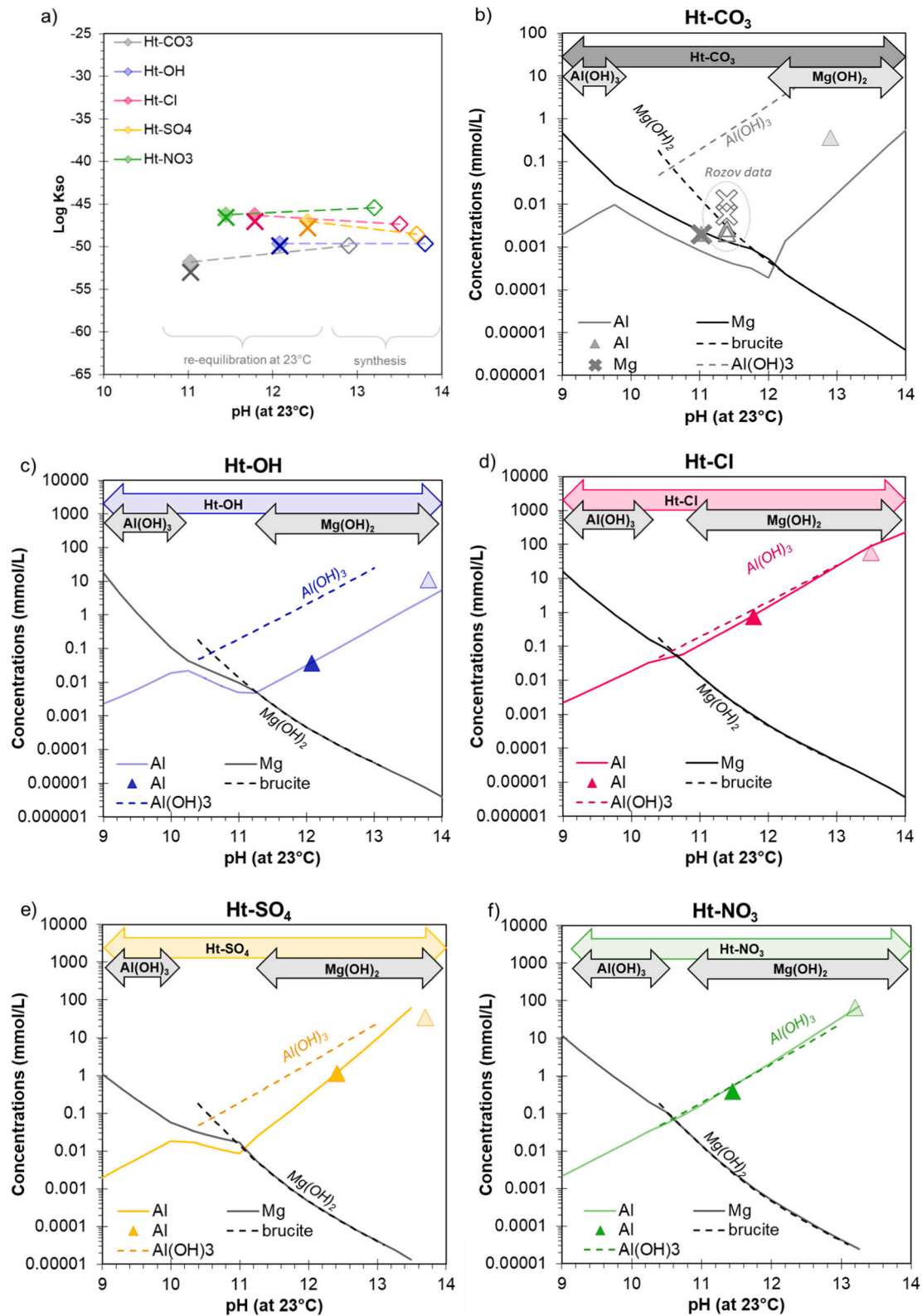


Fig. 7. a) Comparison of the calculated solubility product from oversaturation experiments during synthesis (empty diamonds), calculated solubility product from undersaturation experiments at 23 °C (full diamonds) and solubility products (crosses) corresponding to the data reported in Table 7. Based on the solubility products, magnesium and aluminium concentrations were calculated at equilibrium with the specific hydrotalcite: b) Ht-CO₃, c) Ht-OH, d) Ht-Cl, e) Ht-SO₄, f) Ht-NO₃, as a function of the pH and compared to the experimental data; solubility of brucite and microcrystalline Al(OH)₃ were added for comparison. For b) the experimental data given in [13] were added for comparison.

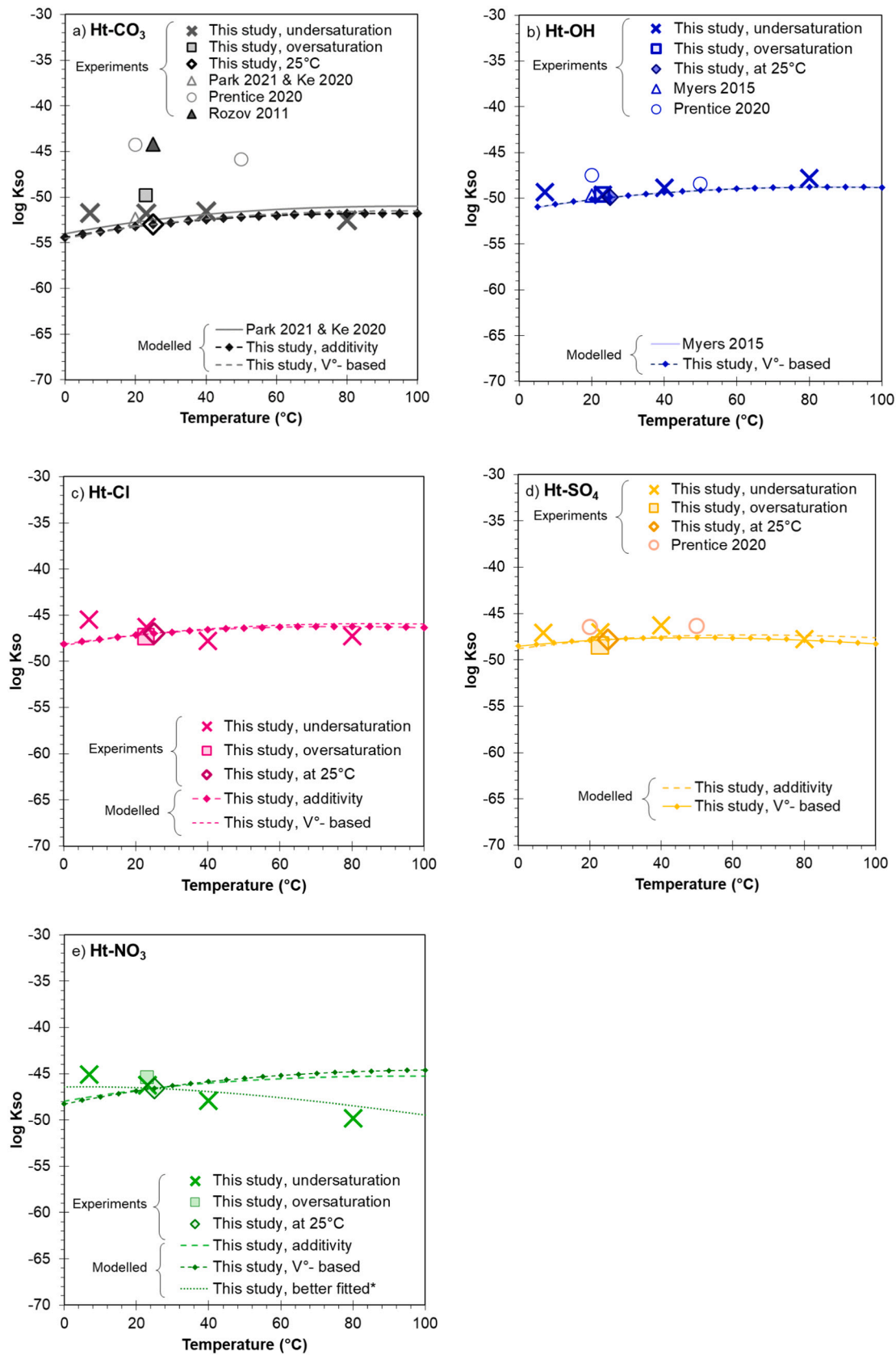


Fig. 8. Solubility products (given in Table 7) as a function of temperature compared to relevant literature (Table 1) and the modelled solubility products are modelled with the S° and C_p° given in Table S 5; a) for $Mg_4Al_2(OH)_{12}(CO_3)_1(H_2O)_4$, b) for $Mg_4Al_2(OH)_{13.8}(CO_3)_{0.1}(H_2O)_4$, c) for $Mg_4Al_2(OH)_{12.7}(Cl)_{0.7}(CO_3)_{0.3}(H_2O)_4$, d) for $Mg_4Al_2(OH)_{11.8}(SO_4)_{0.8}(CO_3)_{0.3}(H_2O)_4$, e) for $Mg_4Al_2(OH)_{12.4}(NO_3)_1(CO_3)_{0.3}(H_2O)_4$; Prentice 2020 data were recalculated from the measured concentrations in [24] assuming Mg concentrations which correspond to brucite solubility and Mg/Al = 2; * = no physical meaning.

measured data [59]. For the Ht-SO₄ and the Ht-NO₃ samples, however, the volume based data were selected due to the approximate nature of the entropies of Mg(NO₃)₂, MgSO₄ given in literature.

However, the changes in the solubility with temperature for the Ht-NO₃ phase were still underestimated (see Fig. 8). Thus, the S° values for this hydrotalcite were fitted based on our experimental solubility values following the procedure described in [58,62].

The log K_{s0} calculated here are comparable to other data reported in literature for Ht-OH, Ht-CO₃ and Ht-SO₄. Only in the case of Ht-CO₃, the solubility products recalculated based on the oversaturation experiments of [12,13] or [24] are considerably higher than the values obtained here from undersaturation experiments, which could indicate a kinetic hindrance in the precipitation of Ht-CO₃. For the Ht-SO₄ phase, the recalculated experimental solubility from [24] assuming Mg in equilibrium with brucite and our data are in good agreement.

From our knowledge, the temperature effect on the solubility of Ht-NO₃ has not been measured before and it showed a steeper decrease than expected. The V_{cell} of 314 Å³ estimated from the fitted S° is large for hydrotalcite and would correspond to a basal spacing of ~13 Å and thus and thus to the presence of 2 or 3 additional water molecules per 2Al in formula in the interlayer. In fact, some studies reported a bigger basal spacing for NO₃-hydrotalcite than in the SO₄-hydrotalcite [14], such that we suspect the presence of CO₃²⁻ in the interlayer (i.e. a higher CO₂ contamination with a higher temperature). The final data given by this study are in bold in Table S5.

3.4.3. Extrapolation to the other Mg/Al ratios

Hydrotalcite phases are part of the LDH group and can have variable M^{2+}/M^{3+} ratios between 2 and 4, although more crystalline structures are observed for the specific M^{2+}/M^{3+} ratios of 2, 3 and 4 [10]. To be able to describe the compositional variation an ideal solid solution was assumed, as previously done [7,12,13] based on end-members with Mg/Al = 2, 3 and 4. The thermodynamic data for the Mg/Al = 2 obtained experimentally in this study were used together with the data for brucite and H₂O (see Table 1) to estimate the solubility products and entropy data for LDH with $Mg^{2+}/Al^{3+} = 3$ and 4 using the additivity method suggested in [7], e.g. for $Mg_6Al_2(OH)_{16}(CO_3)_5 \cdot 5H_2O = Mg_4Al_2(OH)_{12}(CO_3)_4 \cdot 4H_2O + 2 \times Mg(OH)_2 + H_2O$: $\log K(Mg_6Al_2(OH)_{16}(CO_3)_5 \cdot 5H_2O) = \log K(Mg_4Al_2(OH)_{12}(CO_3)_4 \cdot 4H_2O) + 2 \times \log K(Mg(OH)_2) + \log K(H_2O) = -53.0 - 2 \times 11.16 - 0 = -75.32$. This additivity method describes well the strong dependence of the solubility product of hydrotalcite on the high Mg/Al as observed in experimental

investigations [12,13,24]. The molar volumes V° were estimated from the crystal structure: c was kept constant while the increase of a with the (Al/Mg + Al) change was calculated with the relationship given in [11]. The entropy S° and the heat capacity C_p° were deduced based on equations given in Fig. S6. The full thermodynamic data are given in Table 8. The resulting log K_{s0} values are given in Fig. 9 and compiled together with S° and C_p° values in Table 8.

Fig. 9a compares the solubility product of CO₃-hydrotalcite with Mg/Al = 2, 3 and 4 with log K_{s0} values reported in literature [5,12,13,23], and log K_{s0} values recalculated from [14,24,59]. The log K_{s0} calculated in our study are in the same range as most literature values, with the exception of the log K_{s0} for Mg/Al = 2 and 3 given by [12,13] or recalculated from [24], which are several log units higher (less negative). Those solubility data have been obtained from oversaturation experiments. In fact, in the case of CO₃-hydrotalcite all log K_{s0} based on oversaturation experiments [12,13,24] and oversaturation K_{s0} in Table 7 are higher than those obtained from undersaturation experiments (Table 7) or calculated based on the thermodynamic data of other hydrotalcite [14,22–24,59], which could indicate towards a kinetic hindrance in the precipitation of CO₃-hydrotalcite.

The solubility products derived for OH-hydrotalcite Mg/Al = 2, 3 and 4 (containing residual CO₃²⁻) agree very well with the log K_{s0} corresponding to the solid solution given by [7] and reasonably well with the recalculated log K_{s0} based on liquid composition given in [24] or with the OH-hydrotalcite calculated to precipitate in PC [5] as shown in Fig. 9b. We observed experimentally similar values in over- and under-saturation experiments and the values are similar (± 0.5 log10 units) to those calculated in [7] from short term oversaturation experiments, while the data recalculated from [24] were less negative and those from [5] more negative (Table 1). In fact, [21] critically discussed the solubility products suggested for OH-hydrotalcite by Lothenbach et al. (2006) [5] and found that this solubility product for OH-hydrotalcite was too low, without being able to suggest a better value due to the lack of experimental data at that time.

In addition, the Fig. 9c compares the log K_{s0} calculated for the hydrotalcite containing Cl⁻, SO₄²⁻ and NO₃⁻ with the few data found in literature. The values observed here agree well with the log K_{s0} recalculated for the SO₄-hydrotalcite from the solution analysis from [24], the log K_{s0} calculated from [38] for the Cl-hydrotalcite, and the log K_{s0} for NO₃-hydrotalcite reported in [37]. Also the log K_{s0} recalculated from the ion exchange experiments of [14] for the Cl-hydrotalcite and NO₃-hydrotalcite agree well.

Table 8

Tentative thermodynamic properties of the end-members of the hydrotalcite ideal solid solution containing CO₃, OH, Cl, NO₃ and SO₄ at standard conditions (25 °C and 1 atm). Log K_{s0} designates the solubility product with respect to Mg^{2+} , SiO₂, OH⁻, CO₃²⁻, Cl⁻, NO₃⁻, SO₄²⁻ and H₂O; $C_p^\circ = a + bT + cT^{-2} + dT^{-1/2}$.

	log K_{s0} (25 °C) \pm 1.5	$\Delta_f G^\circ$ (kJ/mol)	$\Delta_f H^\circ$ (kJ/mol)	V° (cm ³ /mol)	S° (J/K/mol)	C_p° (J/K/mol)
Mg ₄ Al ₂ (OH) ₁₂ (CO ₃) ₄ ·4H ₂ O	-53.0	-6827.95	-7670.92	222	621 ^a	727 ^a
Mg ₆ Al ₂ (OH) ₁₆ (CO ₃) ₅ ·5H ₂ O	-75.3	-8729.47	-9805.53	301 ^b	810 ^c	953 ^c
Mg ₈ Al ₂ (OH) ₂₀ (CO ₃) ₆ ·6H ₂ O	-97.6	-10,631.00	-11,933.19	380 ^b	1022 ^c	1200 ^c
Mg ₄ Al ₂ (OH) _{13.8} (CO ₃) _{0.1} ·4H ₂ O	-49.9	-6618.16	-7467.82	224	619 ^a	723 ^a
Mg ₆ Al ₂ (OH) _{17.8} (CO ₃) _{0.1} ·5H ₂ O	-72.2	-85,196.8	-9600.10	303 ^b	815 ^c	959 ^c
Mg ₈ Al ₂ (OH) _{21.8} (CO ₃) _{0.1} ·6H ₂ O	-94.5	-10,421.20	-11,727.31	382 ^b	1029 ^c	1209 ^c
Mg ₄ Al ₂ (OH) _{12.7} (Cl) _{0.7} (CO ₃) _{0.3} ·4H ₂ O	-47.0	-6626.02	-7459.68	222	629 ^a	729 ^a
Mg ₆ Al ₂ (OH) _{16.7} (Cl) _{0.7} (CO ₃) _{0.3} ·5H ₂ O	-69.3	-8527.66	-9597.33	300 ^b	808 ^c	950 ^c
Mg ₈ Al ₂ (OH) _{20.7} (Cl) _{0.7} (CO ₃) _{0.3} ·6H ₂ O	-91.6	-10,429.30	-11,725.22	379 ^b	1019 ^c	1197 ^c
Mg ₄ Al ₂ (OH) _{11.8} (SO ₄) _{0.8} (CO ₃) _{0.3} ·4H ₂ O	-47.8	-6992.68	-7836.09	268	721 ^c	848 ^c
Mg ₆ Al ₂ (OH) _{15.8} (SO ₄) _{0.8} (CO ₃) _{0.3} ·5H ₂ O	-70.1	-8894.32	-99,485.55	362 ^b	974 ^c	1145 ^c
Mg ₈ Al ₂ (OH) _{19.8} (SO ₄) _{0.8} (CO ₃) _{0.3} ·6H ₂ O	-92.4	-10,795.84	-12,066.33	457 ^b	1229 ^c	1443 ^b
Mg ₄ Al ₂ (OH) _{12.4} (NO ₃) ₁ (CO ₃) _{0.3} ·4H ₂ O	-46.6	-6595.42	-7515.52	228	614 ^{c, d}	723 ^{c, d}
Mg ₆ Al ₂ (OH) _{16.4} (NO ₃) ₁ (CO ₃) _{0.3} ·5H ₂ O	-68.9	-84,971.67	-9641.82	309 ^b	831 ^c	977 ^c
Mg ₈ Al ₂ (OH) _{20.4} (NO ₃) ₁ (CO ₃) _{0.3} ·6H ₂ O	-91.2	-10,398.70	-11,767.78	390 ^b	1049 ^c	1232 ^c

^a S° estimated from additivity.

^b V° estimated from the crystal structure and the increase of the cell parameter a with Mg/Al described in [11].

^c S° and C_p° estimated from the V° and the equations given in Fig. S6 and Table S5.

^d S° values from the V° -based, do not fit the experimental solubility data with the increase of temperature (Fig. 8e).

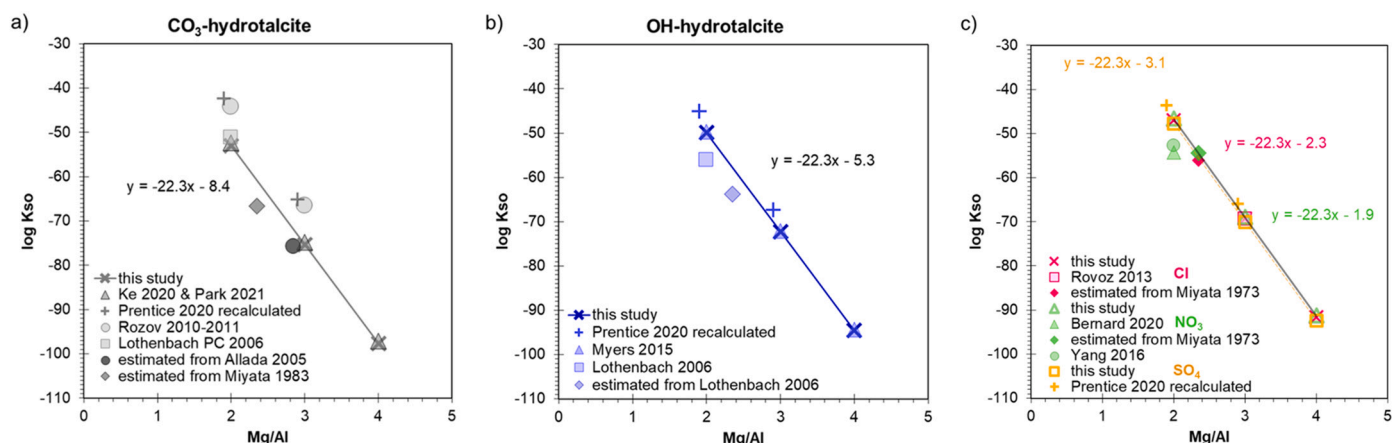


Fig. 9. Solubility products ($\log K_{so}$) for a) CO_3 -hydrotalcite, b) OH -hydrotalcite and c) Cl -hydrotalcite, NO_3 -hydrotalcite, and SO_4 -hydrotalcite (Table 8) compared to $\log K_{so}$ from literature (Table 1) as a function of Mg/Al in hydrotalcite.

While anion substitutions in the structure of hydrotalcite are common [10,14,43,44], hydrotalcite containing CO_3 is the most stable and thus together with OH -hydrotalcite the most probable hydrotalcite formed in cementitious materials, i.e. in the presence of NO_3 , Cl and sulphate concentrations in the millimolar concentration range, as the kind of anions present in hydrotalcite depends strongly on the concentrations. The use of this hydrotalcite provisional ideal solid solution based on the data derived in this study predict the formation of a hydrotalcite containing mainly OH^- in the interlayer in a carbonate free hydrated Portland cement and of a hydrotalcite containing both carbonate and OH^- in a Portland cement containing CaCO_3 . This prediction is in good agreement with the experimental observation of hydrotalcite formation in Mg -rich Portland cements [17]. Cl^- or NO_3^- containing hydrotalcite may be formed in environment containing high Cl^- or NO_3^- concentrations; in fact the formation of chloride containing hydrotalcite has been observed at high chloride concentrations [16].

4. Conclusions

Magnesium present in cementitious materials is experimentally observed to precipitate as poorly crystalline magnesium-based double hydroxide layer phases (LDH) containing aluminium. Such hydrotalcite-like phases can incorporate different anions in the interlayer to compensate the positive main layer charge. In this study, hydrotalcites with different anions, CO_3^{2-} , OH^- , NO_3^- , Cl^- , and SO_4^{2-} in the interlayer were successfully synthesised at 80°C . Mass balance, XRD and FT-IR indicated the incorporation of the respective anion, CO_3^{2-} , OH^- , NO_3^- , Cl^- , and SO_4^{2-} , in the interlayer. In addition, some CO_3^{2-} was present in the interlayer due to the high affinity of hydrotalcite for carbonate. The crystallinity of the hydrotalcites depended on the anion and increased in the order: $\text{SO}_4^{2-} < \text{Cl}^- < \text{NO}_3^- < \text{OH}^- < \text{CO}_3^{2-}$.

In-situ XRD and TGA experiments showed that the basal spacing and the amount of interlayer water decreases stepwise with temperature, and that the amount of interlayer water and the temperature at which this water is lost depends on the incorporated anion.

The solubility products, calculated based on the solution analysis of samples re-equilibrated at 7, 23, 40 and 80°C showed that the CO_3 -hydrotalcite was the most stable hydrotalcite, followed by OH -hydrotalcite, while SO_4 -hydrotalcite, Cl -hydrotalcite and NO_3 -hydrotalcite were less stable. In the case of CO_3 -hydrotalcite a higher solubility was observed in oversaturation experiments than in undersaturation experiments indicating a possible kinetic hindrance in the precipitation of CO_3 -hydrotalcite. Such a kinetic hindrance would also explain the large scatter in literature data in the case of CO_3 -hydrotalcite, where several experimental studies based on oversaturation experiments showed a much higher solubility. For OH^- , SO_4^{2-} , Cl^- and NO_3^-

hydrotalcite no significant difference between the solubility obtained from oversaturation and from undersaturation was observed in our experiments and the data showed reasonable agreement with the few solubility measurements available in literature.

The solubility of the hydrotalcites studied showed only a weak dependence on temperature, similar to the trends observed for Ca - Al -based LDH. The thermodynamic data derived experimentally for hydrotalcite with $\text{Mg}/\text{Al} = 2$ were extrapolated to $\text{Mg}/\text{Al} = 3$ and 4 using a simple additivity method [7], which described the few available literature data well.

Thermodynamic data for hydrotalcite containing OH , CO_3 , SO_4 , Cl and NO_3 are given including, solubility product, molar volume, entropy and heat capacity. This work provides new data that are needed to predict the formation of hydrotalcite in cementitious materials and the use of a provisional ideal solid solution model is suggested. Such a model predicts the formation of hydrotalcite containing carbonate and OH^- in its interlayer if applied to hydrated Portland cement but can also be used for other cementitious materials such as alkali activated cements.

This work gives basis to work with updated and more homogeneous thermodynamic data for pure Mg - Al LDH phases. However, the iron from Portland cement or from industrial wastes (e.g. slags) is also expected to be incorporated in LDH phases, and further work should be conducted to describe the incorporation of Fe in the LDH by thermodynamic modelling and future research is necessary to construct more rigorous and quantitative solid solution model.

Supplementary data to this article can be found online at <https://doi.org/10.1016/j.cemconres.2021.106674>.

CRediT authorship contribution statement

Ellina Bernard: Conceptualization; Methodology; Formal analysis; Investigation; Validation; Writing – original draft. **Wolfgang Jan Zucha:** Formal analysis; Investigation; Writing – review & editing. **Barbara Lothenbach:** Supervision; Investigation; Validation; Writing – review & editing. **Urs Mäder:** Supervision; Resources; Writing – review & editing.

Declaration of competing interest

The authors declare that they have no known competing financial interests or personal relationships that could have appeared to influence the work reported in this paper.

Acknowledgements

The authors would like to thank Dr. Daniel Rentsch (Empa) for NMR

analyses. Priska Baehler, Christopher Pichler and Dr. Niklaus Waber (UniBern) are acknowledged for the solution analyses. Yiru Yan and Rosa Guidone (Empa) for help with the TGA-FT-IR measurements, Dr. Urs Eggenberger (UniBern) for giving access to measuring setups. The helpful insights from the two anonymous reviewers are thankfully acknowledged.

The research leading to these results has received funding from the European Union's Horizon 2020 Research and Training Programme of the European Atomic Energy Community (EURATOM) (H2020-NFRP-2014/2015) under grant agreement n° 662147 (CEBAMA).

References

- [1] S.A. Miller, A. Horvath, P.J. Monteiro, Readily implementable techniques can cut annual CO₂ emissions from the production of concrete by over 20%, *Environ. Res. Lett.* 11 (2016), 074029.
- [2] B. Lothenbach, K. Scrivener, R. Hooton, Supplementary cementitious materials, *Cem. Concr. Res.* 41 (2011) 1244–1256.
- [3] M.B. Haha, B. Lothenbach, G. Le Saout, F. Winnefeld, Influence of slag chemistry on the hydration of alkali-activated blast-furnace slag—part I: effect of MgO, *Cem. Concr. Res.* 41 (2011) 955–963.
- [4] B. Lothenbach, G. Le Saout, E. Gallucci, K. Scrivener, Influence of limestone on the hydration of Portland cements, *Cem. Concr. Res.* 38 (2008) 848–860.
- [5] B. Lothenbach, F. Winnefeld, Thermodynamic modelling of the hydration of Portland cement, *Cem. Concr. Res.* 36 (2006) 209–226.
- [6] S.A. Bernal, R. San Nicolas, R.J. Myers, R.M. de Gutiérrez, F. Puertas, J.S. van Deventer, J.L. Provis, MgO content of slag controls phase evolution and structural changes induced by accelerated carbonation in alkali-activated binders, *Cem. Concr. Res.* 57 (2014) 33–43.
- [7] R.J. Myers, B. Lothenbach, S.A. Bernal, J.L. Provis, Thermodynamic modelling of alkali-activated slag cements, *Appl. Geochem.* 61 (2015) 233–247.
- [8] S. Park, H.M. Park, H. Yoon, J. Seo, C.-M. Yang, J.L. Provis, B. Yang, Hydration kinetics and products of MgO-activated blast furnace slag, *Constr. Build. Mater.* 249 (2020), 118700.
- [9] S.M. Park, J. Jang, H.-K. Lee, Unlocking the role of MgO in the carbonation of alkali-activated slag cement, *Inorg. Chem. Front.* 5 (2018) 1661–1670.
- [10] S.J. Mills, A.G. Christy, J.-M. Génin, T. Kameda, F. Colombo, Nomenclature of the hydrotalcite supergroup: natural layered double hydroxides, *Mineral. Mag.* 76 (2012) 1289–1336.
- [11] I.G. Richardson, Clarification of possible ordered distributions of trivalent cations in layered double hydroxides and an explanation for the observed variation in the lower solid-solution limit, *Acta Crystallogr. Sect. B: Struct. Sci. Cryst. Eng. Mater.* 69 (2013) 629–633.
- [12] K. Rozov, U. Berner, D. Kulik, L.W. Diamond, Solubility and thermodynamic properties of carbonate-bearing hydrotalcite-pyroxaurite solid solutions with a 3:1 Mg/(Al+Fe) mole ratio, *Clay Clay Miner.* 59 (2011) 215–232.
- [13] K. Rozov, U. Berner, C. Taviot-Gueho, F. Leroux, G. Renaudin, D. Kulik, L. W. Diamond, Synthesis and characterization of the LDH hydrotalcite-pyroxaurite solid-solution series, *Cem. Concr. Res.* 40 (2010) 1248–1254.
- [14] S. Miyata, Anion-exchange properties of hydrotalcite-like compounds, *Clay Clay Miner.* 31 (1983) 305–311.
- [15] F. Cavani, F. Trifiro, A. Vaccari, Hydrotalcite-type anionic clays: preparation, properties and applications, *Catal. Today* 11 (1991) 173–301.
- [16] X. Ke, S.A. Bernal, J.L. Provis, Uptake of chloride and carbonate by mg-Al and ca-Al layered double hydroxides in simulated pore solutions of alkali-activated slag cement, *Cem. Concr. Res.* 100 (2017) 1–13.
- [17] A. Machner, M. Zajac, M.B. Haha, K.O. Kjellsen, M.R. Geiker, K. De Weert, Chloride-binding capacity of hydrotalcite in cement pastes containing dolomite and metakaolin, *Cem. Concr. Res.* 107 (2018) 163–181.
- [18] E. Bernard, A. Jenni, M. Fisch, D. Grolimund, U. Mäder, Micro-X-ray diffraction and chemical mapping of aged interfaces between cement pastes and opalinus clay, *Appl. Geochem.* 115 (2020), 104538.
- [19] U. Mäder, A. Jenni, C. Lerouge, S. Gaboreau, S. Miyoshi, Y. Kimura, V. Cloet, M. Fukaya, F. Claret, T. Otake, M. Shibata, B. Lothenbach, 5-year chemico-physical evolution of concrete-claystone interfaces, *Swiss J. Geosci.* 110 (2017) 307–327.
- [20] E. Bernard, B. Lothenbach, D. Rentsch, Influence of sodium nitrate on the phases formed in the MgO-Al₂O₃-SiO₂-H₂O system, *Mater. Des.* 198 (2021), 109391.
- [21] B. Lothenbach, D.A. Kulik, T. Matschei, M. Balonis, L. Baquerizo, B. Dilnesa, G. D. Miron, R.J. Myers, Cemdata18: a chemical thermodynamic database for hydrated Portland cements and alkali-activated materials, *Cem. Concr. Res.* 115 (2019) 472–506.
- [22] X. Ke, S.A. Bernal, J.L. Provis, B. Lothenbach, Thermodynamic modelling of the phase evolution in alkali-activated slag cements exposed to carbon dioxide, *Cem. Concr. Res.* 136 (2020), 106158.
- [23] S. Park, B. Lothenbach, J.G. Jang, H.K. Kim, N. Lee, Thermodynamic modelling and experimental study of hydration and carbonation of alkali activated slag cements, *Cem. Concr. Compos.* (2021) submitted.
- [24] D.P. Prentice, L. Gomez-Zamorano, M. Balonis, B. Erdemli, K. Ellison, N. Neithalath, D. Simonetti, G. Sant, The effects of (di-, tri-valent)-cation partitioning and intercalant anion-type on the solubility of hydrotalcites, *J. Am. Ceram. Soc.* 103 (10) (2020) 6025–6039.
- [25] S. Brunauer, P.H. Emmett, E. Teller, Adsorption of gases in multimolecular layers, *J. Am. Chem. Soc.* 60 (1938) 309–319.
- [26] D. Massiot, F. Fayon, M. Capron, I. King, S. Le Calvé, B. Alonso, J.O. Durand, B. Bujoli, Z. Gan, G. Hoatson, Modelling one- and two-dimensional solid-state NMR spectra, *Magn. Reson. Chem.* 40 (2002) 70–76.
- [27] D.R. Neuville, L. Cormier, D. Massiot, Al environment in tectosilicate and peraluminous glasses: a 27Al MQ-MAS NMR, raman, and XANES investigation, *Geochim. Cosmochim. Acta* 68 (2004) 5071–5079.
- [28] D. Kulik, T. Wagner, S.V. Dmytrieva, G. Kosakowski, F. Hingerl, K.V. Chudnenko, U. Berner, GEM-Selektor geochemical modeling package: revised algorithm and GEMS3K numerical kernel for coupled simulation codes, *Comput. Geochem.* 17 (2013) 1–24.
- [29] T. Thoenen, W. Hummel, U. Berner, E. Curti, The PSI/Nagra Chemical Thermodynamic Database 12/07, PSI report 14-04, Villigen PSI, Switzerland, 2014.
- [30] B. Lothenbach, L. Pelletier-Chaignat, F. Winnefeld, Stability in the system CaO-Al₂O₃-H₂O, *Cem. Concr. Res.* 42 (2012) 1621–1634.
- [31] W. Gao, Z. Li, Solubility and KSP of Mg₄Al₂(OH)₁₄·3H₂O at the various ionic strengths, *Hydrometallurgy* 117 (2012) 36–46.
- [32] H.C. Helgeson, Summary and critique of the thermodynamic properties of rock-forming minerals, *Am. J. Sci.* 278 (1978) 1–229.
- [33] R.A. Robie, B.S. Hemingway, Thermodynamic Properties of Minerals and Related Substances at 298.15 K and 1 Bar (105 Pascals) Pressure and at Higher Temperatures, US Government Printing Office, 1995.
- [34] M. Weil, The high-temperature modification of magnesium sulfate (β-MgSO₄) from single-crystal data, *Acta Crystallogr. Sect. E: Struct. Rep. Online* 63 (2007), i172–i172.
- [35] P. Blanc, X. Bourbon, A. Lassin, E.C. Gaucher, Chemical model for cement-based materials: thermodynamic data assessment for phases other than C-S-H, *Cem. Concr. Res.* 40 (2010) 1360–1374.
- [36] C. Johnson, F. Glasser, Hydrotalcite-like minerals (M₂Al(OH)₆(CO₃) 0.5. XH₂O, where M = Mg, Zn, Co, Ni) in the environment: synthesis, characterization and thermodynamic stability, *Clay Clay Miner.* 51 (2003) 1–8.
- [37] P. Yang, A. Yamagishi, H. Sato, Thermodynamic approach for formation of layered double hydroxides: effects of intercalated anions, *Clay Sci.* 20 (2016) 27–30.
- [38] K. Rozov, H. Curtius, A. Neumann, D. Bosbach, Synthesis, characterization and stability properties of cl-bearing hydrotalcite-pyroxaurite solids, *Radiochim. Acta* 101 (2013) 101–110.
- [39] G.M. Anderson, D.A. Crerar, Thermodynamics in Geochemistry: The Equilibrium Model, Oxford University Press, Oxford, 1993.
- [40] D.A. Kulik, Minimising uncertainty induced by temperature extrapolations of thermodynamic data: a pragmatic view on the integration of thermodynamic databases into geochemical computer codes, in: Organisation for Economic Co-Operation and Development - Nuclear Energy Agency, Nuclear Energy Agency of the OECD (NEA), 2002.
- [41] S. Miyata, The syntheses of hydrotalcite-like compounds and their structures and physico-chemical properties—I: the systems Mg₂+Al₃+NO₃–, Mg₂+Al₃+Cl–, Mg₂+Al₃+ClO₄–, Ni₂+Al₃+Cl– and zn₂+Al₃+Cl–, *Clay Clay Miner.* 23 (1975) 369–375.
- [42] C. Liu, M. Zhang, G. Pan, L. Lundehøj, U.G. Nielsen, Y. Shi, H.C.B. Hansen, Phosphate capture by ultrathin MgAl layered double hydroxide nanoparticles, *Appl. Clay Sci.* 177 (2019) 82–90.
- [43] V.R. Constantino, T.J. Pinnavaia, Basic properties of Mg₂+1-xAl₃+x layered double hydroxides intercalated by carbonate, hydroxide, chloride, and sulfate anions, *Inorg. Chem.* 34 (1995) 883–892.
- [44] J.T. Klopogge, J. Kristóf, R.L. Frost, Thermogravimetric analysis-mass spectrometry (TGA-MS) of hydrotalcites containing CO₃²⁻, NO₃⁻, Cl⁻, SO₄²⁻ or ClO₄⁻, in: Proceedings of the 12th International Clay Conference, Elsevier, Bahía Blanca, Argentina, 2001.
- [45] V.R. Constantino, T.J. Pinnavaia, Structure-reactivity relationships for basic catalysts derived from a Mg₂+Al₃+CO₃– layered double hydroxide, *Catal. Lett.* 23 (1994) 361–367.
- [46] K.J. MacKenzie, R.H. Meinhold, B.L. Sherriff, Z. Xu, 27 Al and 25 mg solid-state magic-angle spinning nuclear magnetic resonance study of hydrotalcite and its thermal decomposition sequence, *J. Mater. Chem.* 3 (1993) 1263–1269.
- [47] A.O. Sjöstad, N.H. Andersen, P. Vajeeston, J. Karthikeyan, B. Arstad, A. Karlsson, H. Fjellvåg, On the thermal stability and structures of layered double hydroxides Mg_{1-x}Al_x(OH)₂(NO₃)_x·mH₂O (0.18 ≤ x ≤ 0.38), *Eur. J. Inorg. Chem.* 2015 (2015) 1775–1788.
- [48] Z. Zhang, Y. Zheng, Y. Ni, Z. Liu, J. Chen, X. Liang, Temperature- and pH-dependent morphology and FT–IR analysis of magnesium carbonate hydrates, *J. Phys. Chem. B* 110 (2006) 12969–12973.
- [49] M.R. Rosenthal, The myth of the non-coordinating anion, *J. Chem. Educ.* 50 (1973) 331.
- [50] S.-L. Wang, P.-C. Wang, In situ XRD and ATR-FTIR study on the molecular orientation of interlayer nitrate in Mg/Al-layered double hydroxides in water, *Colloids Surf. A Physicochem. Eng. Asp.* 292 (2007) 131–138.
- [51] E. Lippmaa, A. Samoson, M. Magi, High-resolution aluminum-27 NMR of aluminosilicates, *J. Am. Chem. Soc.* 108 (1986) 1730–1735.
- [52] T. Hibino, A. Tsunashima, Characterization of repeatedly reconstructed Mg–Al hydrotalcite-like compounds: gradual segregation of aluminum from the structure, *Chem. Mater.* 10 (1998) 4055–4061.
- [53] H. Maekawa, T. Nakao, S. Shimokawa, T. Yokokawa, Coordination of sodium ions in NaAlO₂-SiO₂ melts: a high temperature 23 Na NMR study, *Phys. Chem. Miner.* 24 (1997) 53–65.

- [54] R. Tabeta, M. Aida, H. Saitô, A high-resolution solid-state ^{23}Na NMR study of sodium complexes with solvents, small ligand molecules, and ionophores. ^{23}Na chemical shifts as means for identification and characterization of ion-ion, ion-solvent, and ion-ligand interactions, *Bull. Chem. Soc. Jpn.* 59 (1986) 1957–1966.
- [55] B. Lothenbach, P. Durdzinski, K. DeWeerd, Thermogravimetric analysis, in: K. Scrivener, R. Snellings, B. Lothenbach (Eds.), *A Practical Guide to Microstructural Analysis of Cementitious Materials*, CRC Press, Oxford, UK, 2016, pp. 177–212.
- [56] M. Laine, Y. Liao, F. Varenne, P. Picot, L.J. Michot, E. Barruet, V. Geertsen, A. Thill, M. Pelletier, J.-B. Brubach, Tuning the nature of the anion in hydrated layered double hydroxides for H_2 production under ionizing radiation, *ACS Appl. Nano Mater.* 1 (2018) 5246–5257.
- [57] C. Appelo, The anion exchange properties of AFm (hydrocalumite-group) minerals defined from solubility experiments and crystallographic information, *Cem. Concr. Res.* 140 (2021), 106270.
- [58] T. Matschei, B. Lothenbach, F.P. Glasser, Thermodynamic properties of Portland cement hydrates in the system $\text{CaO}-\text{Al}_2\text{O}_3-\text{SiO}_2-\text{CaSO}_4-\text{CaCO}_3-\text{H}_2\text{O}$, *Cem. Concr. Res.* 37 (2007) 1379–1410.
- [59] R.K. Allada, J.D. Pless, T.M. Nenoff, A. Navrotsky, Thermochemistry of hydrotalcite-like phases intercalated with CO_3^{2-} , NO_3^- , Cl^- , I^- , and ReO_4^- , *Chem. Mater.* 17 (2005) 2455–2459.
- [60] S. Ghazizadeh, T. Hanein, J.L. Provis, T. Matschei, Estimation of standard molar entropy of cement hydrates and clinker minerals, *Cem. Concr. Res.* 136 (2020), 106188.
- [61] L. Glasser, The effective volumes of waters of crystallization & the thermodynamics of cementitious materials, *Cement* 3 (2021), 100004.
- [62] B. Lothenbach, T. Matschei, G. Möschner, F.P. Glasser, Thermodynamic modelling of the effect of temperature on the hydration and porosity of Portland cement, *Cem. Concr. Res.* 38 (2008) 1–18.